Title

Subsurface flow in lowland river gravel bars

Journal

Water Resources Research, 53(9)

ISSN

0043-1397

Authors

Bray, EN

Dunne, T

Publication Date

2017-09-01

DOI

10.1002/2016wr019514

Peer reviewed

AGU PUBLICATIONS

Water Resources Research

RESEARCH ARTICLE
10.1002/2016WR019514

Subsurface flow in lowland river gravel bars

E. N. Bray[1,2] and T. Dunne[3]

[1]Earth Research Institute, University of California, Santa Barbara, California, USA, [2]Center for Environmental Design Research, University of California, Berkeley, California, USA, [3]Bren School of Environmental Science and Management, University of California, Santa Barbara, California, USA

Key Points:
- An analytical bedform-infiltration relation shows that infiltration areas are controlled by sinusoidal or irregular, asymmetric bed topography
- Streambed hydraulic conductivity varies by orders of magnitude along riffle-pool sequences related to bar evolution
- The range and spatial pattern in K relative to morphologic features strongly controls hyporheic residence times

Supporting Information:
- Supporting Information S1

Correspondence to:
E. Bray,
ebray@bren.ucsb.edu

Citation:
Bray, E. N. and T. Dunne (2017), Subsurface flow in lowland river gravel bars, *Water Resour. Res.*, *53*, doi:10.1002/2016WR019514.

Received 18 JUL 2016
Accepted 24 JUL 2017
Accepted article online 1 AUG 2017

Abstract Geomorphic and hydraulic processes, which form gravel bars in large lowland rivers, have distinctive characteristics that control the magnitude and spatial patterns of infiltration and exfiltration between rivers and their immediate subsurface environments. We present a bedform-infiltration relation together with a set of field measurements along two reaches of the San Joaquin River, CA to illustrate the conditions required for infiltration and exfiltration of flow between a stream and its undulating bed, and a numerical model to investigate the factors that affect paths and residence times of flow through barforms at different discharges. It is shown that asymmetry of bar morphology is a first-order control on the extent and location of infiltration, which would otherwise produce equal areas of infiltration and exfiltration under the assumption of sinusoidal bedforms. Hydraulic conductivity varies by orders of magnitude due to fine sediment accumulation and downstream coarsening related to the process of bar evolution. This systematic variability not only controls the magnitude of infiltration, but also the residence time of flow through the bed. The lowest hydraulic conductivity along the reach occurred where the difference between the topographic gradient and the water-surface gradient is at a maximum and thus where infiltration would be greatest into a homogeneous bar, indicating the importance of managing sand supply to maintain the ventilation and flow through salmon spawning riffles. Numerical simulations corroborate our interpretation that infiltration patterns and rates are controlled by distinctive features of bar morphology.

1. Geomorphic Dependence of Subsurface Flow

Undulations in the topography of lowland gravel bed rivers arise due to interactions between the flow and sediment supply and commonly lead to bar and pool morphology variably mantled with gravel and sand [*Leopold*, 1992; *Milne*, 1982]. The flow of river water over an undulating bed creates spatial variations in hydraulic head at the bed surface that drive infiltration, throughflow, and exfiltration of surface water through the shallow subsurface [*Savant et al*., 1987; *Vittal et al*., 1977]. Thus, geomorphic processes influence hydrologic exchange along riverbeds, whose hyporheic processes are important for sustaining intragravel temperature [*Alderdice and Velsen*, 1978; *Beacham and Murray*, 1990; *Geist et al*., 2006], oxygen [*Ingendahl*, 2001; *Wickett*, 1954] and sediment [*Greig et al*., 2005; *Hanrahan et al*., 2005; *Kondolf*, 2000; *Kondolf*, 2000; *Lapointe et al*., 2004; *Suttle et al*., 2004] conditions required for spawning and embryo survival of anadromous and resident fish [*Geist and Dauble*, 1998; *Tonina and Buffington*, 2009b]. The spatial pattern and rate of infiltration are controlled by the spatially varying interactions of the water surface and the topography and sedimentology of the bed [*Tonina and Buffington*, 2009a]. Understanding these interactions facilitates prediction of hyporheic fluxes of water and ventilation of the subsurface [*Edwards*, 1998], and of whether management of streamflow or sediment supply might improve the quality of salmonid spawning and incubation habitats.

While many studies of shallow subsurface or "hyporheic" flow at bedform-to-reach scales have focused in steep headwater river channels, lowland gravel bed reaches have received less attention and differ in several ways. First, they have larger drainage areas and gentler bed slopes, which together cause the ratio of the flow depth to the grain size and even to bedform amplitude to be large. Thus, transport capacities are usually high enough to entrain a portion of the bed material during bankfull events [*Konrad et al*., 2002; *Leopold*, 1992; *Reid and Dunne*, 2003] whereas bed material in headwater reaches may commonly be mobilized when debris jams fail [*Mosley*, 1981] or during large floods or debris flows [*Yager et al*., 2007]. Second, disruption of alongstream trends in sediment sorting and diminished sediment transport capacity

frequently leads to accumulation of fine sediment on the bed [*Evans and Wilcox*, 2014; *Kondolf and Wilcock*, 1996] and bed surface armoring which persists under even fully mobile conditions [*Church et al*., 1998; *Parker and Sutherland*, 1990; *Wilcock and De Temple*, 2005]. Further, diminished sediment supply downstream of dams causes changes in bedform morphology and confines zones of active bedload transport to a narrow, finer surface bordered by a coarse, less active bed [*Dietrich et al*., 1989]. Finally, bed material in headwater reaches is expected to be coarser as the altitude increases and so also is the hydraulic conductivity expected to increase [*Barontini et al*., 2005]. While recent studies on the hyporheic zone have shown that (1) large rivers play a key role in hyporheic exchange and biogeochemical cycling, (2) the total exchange is dominated by vertical exchange driven by emergent barform features [*Gomez-Velez and Harvey*, 2014], and (3) the thickness of alluvium in gravel bed rivers has a substantial effect on hyporheic flow [*Tonina and Buffington*, 2011], few studies have investigated vertical hyporheic exchange in such environments. In this paper we examine how some of these distinct differences affect infiltration patterns and vertical hyporheic flow fields in lowland gravel bed rivers.

The convex portions of stream surface profiles have traditionally been interpreted to be areas where infiltration (or downwelling) occurs while the concave portions of the stream surface is where exfiltration (or upwelling) occurs. This recognition emerged from theory by *Vaux*, based on the approximation of head fluctuations by a curved water surface parallel to a bed [*Vaux*, 1962]. He demonstrated for a stream without bedforms that downwelling will occur if the bed gradient, hydraulic conductivity, or hyporheic aquifer depth increase in the downstream direction, and upwelling will occur under the opposite circumstances of bed concavity, downstream reduction in hydraulic conductivity or substrate depth. Because Vaux' mathematical model considered no bedforms, it predicted infiltration only where a curve or step in the bed profile created convexity on a parallel water surface. The parallel water surface assumption leads to an infiltration depth and magnitude that are set by the thickness of the aquifer with the primary mechanism of exchange being the curvature-driven exchange.

Subsequent studies demonstrated that bedform topography is a key factor in controlling infiltration and exfiltration and elicited different suggestions concerning the controls to exchange rates and residence times of the hyporheic flow field. It is commonly assumed that the head fluctuations due to bed topography or water surface can be approximated by periodic or idealized sinusoidal waves on an average streambed elevation that is assumed to be a flat or tilted plane (e.g., dune-like bedforms [*Cardenas et al*., 2004]). Alternatively, studies have measured head fluctuations directly in flumes constructed of regular, periodic wavelengths (e.g., riffle-pool sequences [*Tonina and Buffington*, 2011]). The periodic bed assumption leads to an infiltration extent that is typically thought to depend on bedform wavelength and amplitude. It has been shown that areas of the riverbed with high pressure are characterized by downwelling fluxes in which surface water enters the sediment, and low pressure areas exhibit upwelling in which subsurface water enters the river [*Savant et al*., 1987; *Tonina and Buffington*, 2011; *Vittal et al*., 1977]. This has led to general acceptance that in hydrostatic conditions water enters the bed where the water surface slope steepens and exits where the water surface slope lessens [*Boano et al*., 2014]. Further understanding was gained by modeling studies of three-dimensional gravel bedforms. *Marzadri et al*. [2010] and *Tonina and Buffington* [2011] showed that the thickness of alluvium did not control the location or extent of upwelling or downwelling, but that the thickness of alluvium and bar amplitude was an important control to residence time distributions. In both studies, the wavelength of the bed topography was defined to be periodic. At present, no current analytical model accounts for irregular bed topography. The lack of simple theory or model makes it difficult to estimate the position and extent of a natural streambed over which infiltration is possible, leaving open the question of where and over what extent infiltration and hyporheic flow occur.

The rate of infiltration and the depth of flow penetration into the subsurface are also affected by spatial variations in the hydraulic conductivity of the sediment, which can be largely random or associated with the form, genesis and history of the bedforms. Hydraulic conductivity (K) has multiple orders of magnitude of variation, is scale-dependent, and there appears to be little consensus about how to measure it. There is a paucity of field measurements of saturated streambed K (Table 1) and methods have included constant head tests [*Barnard and McBain*, 1994; *Landon et al*., 2001; *Stillwater Sciences*, 2007], constant head injection tests [*Cardenas and Zlotnik*, 2003], falling head slug tests [*Chen*, 2000; *Conant et al*., 2004; *Genereux et al*., 2008; *Kasahara and Wondzell*, 2003; *Rosenberry and Pitlick*, 2009; *Shope et al*., 2012; *Stewardson et al*., 2016; *Wang et al*., 2016], rising head slug tests [*Arntzen et al*., 2006; *Hanrahan et al*., 2005; *Lautz and Siegel*, 2006;

Table 1. Literature Values of Streambed Hydraulic Conductivity (K) for a Range of Fluvial Environments Represented by Previous Studies on Groundwater-Surface Water Exchange or Intragravel Flow

Literature Cited	Site	Gradient (m m^{-1})	K (m d^{-1})
Measured in Gravel—Field			
Barnard and McBain [1994]	McCloud R., Trinity R., Tuolumne R., Freshwater Creek, CA, USA	[a]	~ 48 < 24,000
Stillwater Sciences [2007]	Sacramento River, CA, USA	0.0001–0.001	150–2,900
Leek et al. [2009]	Touchet River, Southeastern WA, USA	0.008–0.012	< 1–1,000
Hanrahan et al. [2005]	Snake River, ID, USA	[a]	2.6–122
Kasahara and Wondzell [2003]	Lookout Creek, Western Cascades, OR, USA	0.01 - 0.14	17.3–86.4
Wang et al. [2016]	Weihe River, Shaanxi Province, Chine	[a]	5.9×10^{-4}–61.3
Rosenberry and Pitlick [2009]	South Platte River, CO, USA	[a]	32–107
Stewardson et al. [2016]	Multiple rivers, France	[a]	<1–49
Measured in Gravel—Flume			
Packman et al. [2004]	Commercial pea gravel, cleaned, experimental flume	0.0009	12,960
Tonina and Buffington [2007]	Gravel, experimental flume	0.002–0.004	4,320
Calculated From Tracer Studies			
Harvey and Bencala [1993]	St. Kevin Gulch, Rocky Mountains, CO, USA	0.067	9.5
Storey et al. [2003]	Speed River, Southern Ontario, CA	0.002–0.005	0.864–8.64
Hatch et al. [2010]	Pajaro River, Central Coast, CA, USA	0.01	8.64
Measured in Sand—Field			
Chen [2000]	Republican River, NE, USA	[a]	18.7–43.0
Genereux et al. [2008]	West Bear Creek, NC, USA	[a]	0.01–66
Lautz and Siegel [2006]	Red Canyon Creek, Rocky Mountains, WY, USA	0.02	0.26–0.86
Cardenas and Zlotnik [2003a]	Prairie Creek, South Platte River, NE, USA	[a]	0.15–74.7
Landon et al. [2001]	North Platte, Platte River and Tributaries, NE, USA	0.0008–0.0014	~5–380
Measured in Sand—Flume			
Salehin et al. [2004]	Sand, cleaned, experimental flume	[a]	17.5–3,690
Assigned			
Cardenas et al. [2004]	Prairie Creek, South Platte River, NE, USA	0.001–0.01	2.5–52.5
Boano et al. [2007]	Simulated sand dunes	0.0001	8.64
Sawyer and Cardenas [2009]	Simulated climbing ripple deposits	0.0001–0.0002	0.84–84

[a]Not reported.

Leek et al., 2009], measurement of seepage and hydraulic gradient to calculate K [*Rosenberry et al*., 2016], and indirect methods based on streambed temperature patterns [*Hatch et al*., 2010]. *Landon et al*. [2001] compared different measurement methods in sand-bedded reaches of the Platte River Basin and found that spatial variations in K were greater than variations between methods, suggesting that the method used matters less than characterizing the spatial variations adequately. Owing to the difficulty of measuring K in the field, several researchers have measured it in laboratory flumes [*Packman et al*., 2004; *Salehin et al*., 2004; *Tonina and Buffington*, 2007] and others have simply assigned values in models [*Boano et al*., 2007; *Gomez-Velez et al*., 2014; *Sawyer and Cardenas*, 2009]. While studies on streambed exchange have explored a range of settings and parameter space, direct measurements of K have extended to the geometry and sedimentology of small steep upland streams, sand-bed streams, or laboratory-constructed channels, but only few to gravel bed lowland rivers.

Besides its strongly varying magnitude, streambed hydraulic conductivity is widely reported to have two other important features: (a) strong spatial variability, and (b) characteristic vertical patterns. Approaches to addressing spatial heterogeneity have included systematic analyses of the statistical effects of heterogeneity in sand-bedded streams by *Tonina et al*. [2016] and *Hester et al*. [2013]. Other approaches have been mostly limited to flume experiments and modeling focused predominantly on sand-bedded dunes and ripples. For example, *Salehin et al*. [2004] showed for flume-constructed bedforms with lognormally correlated random permeabilities that heterogeneity favored horizontal flow and limited the vertical extent of infiltration, resulting in increased fluxes and decreased residence time distributions and hyporheic depth. Flow simulations by *Cardenas et al*. [2004] showed that heterogeneity resulted in both increases and decreases in residence times when compared to a homogenous domain, inducing more vertical flow components. Despite reviews suggesting that heterogeneity tends to increase hyporheic flow [*Boano et al*., 2014, pg. 606], simulations of small-scale exchange in climbing sand ripples by *Sawyer and Cardenas* [2009] and *Bardini et al. [*2013*]*, who employed the same heterogeneous permeability fields, concluded the opposite. Both studies reported that despite the irregular flow patterns, and deeper and longer flow paths arising

from heterogeneity, the residence time distributions were fairly similar to those of their equivalent homogenous media. In the case of *Sawyer and Cardenas* [2009], however, the reduction in exchange flux was an artifact of the approach used to determine an equivalent homogenous medium rather than of the heterogeneity itself. *Bardini et al*. [2013] further concluded that bedform scale heterogeneity typical of lowland rivers did not alter residence time distributions, though it is unknown whether the sandy conditions considered in their investigation are applicable to the broader range of sedimentological conditions in lowland rivers.

Approaches to addressing vertical variations in K are more common, particularly in model simulations that assume a layered field of hydraulic conductivities that exhibit decreases with depth [*Storey et al*., 2003] or exponential decay with depth [*Zlotnik et al*., 2011]. Field measurements suggest the assumed vertical decay in K values was realistic in kind, if not magnitude. For example, *Stillwater Sciences* [2007] measured K *in situ* at depths of 15, 30 and 45 cm in riffles of the gravel-bed Sacramento River (CA); their highest values were at 15 cm and decreased with increasing depth. *Leek et al*. [2009] documented a smoother vertical gradient in K between $\sim$1 m d^{-1} and 1,000 m d^{-1} between depths of 1.35 m and 0.3 m, and showed variability over three orders of magnitude between sampling sites on the Touchet River (WA). *In situ* K measurements taken at depths of $\leq$ 12.5 cm in a cobble bed stream with pore spaces filled by fine sediment showed significant vertical variation (10 – 2,868 m d^{-1}) with generally higher K near the surface [*Ryan and Boufadel*, 2006]. This trend agrees with measurements taken over a deeper interval (1.1 – 1.8 m) in a gravel bed reach of the Truckee River with K ranging from 0.005 to 18.7 m d^{-1} [*Shope et al*., 2012]. However, neither group computed the consequences of these vertical patterns of K in gravel bed rivers on flow circulation within and underneath the streambed profiles.

Collectively, these observations suggest that, aside from the bed topography, the hydraulic conductivity is the most important control on hyporheic flux and residence times through barforms, and thus observations are needed to understand its patterns in relation to topography. Field studies that have directly documented heterogeneity in K at bedform-to-reach scales are rare [*Kennedy et al*., 2009] and none have depicted variations relative to morphology. Nonetheless, the flume studies investigating sediment patterns in bedforms have documented the tendency for vertical sorting [*Blom et al*., 2003], layering of sediments [*Packman et al*., 2006] as well as stratified beds [*Marion et al*., 2008] where it was shown that the coarse armor layer resulted in decreases in residence times and increases in averaged flux rates. The few studies that have evaluated the effects of low-permeability layers included a flume experiment by *Packman and MacKay* [2003] investigating the effects of the deposition of kaolinite clay in a sand bed, and a modeling experiment by *Gomez-Velez et al*. [2014], who found that low permeability layers in small-scale dune bedforms induced stagnation zones with long residence times between surface water and deeper groundwater. In the absence of a consensus about the fundamental nature of heterogeneity in K, its influence to hyporheic flow remains largely unexplored, particularly in gravel bed lowland rivers.

A concept that quantitatively describes hydrologic exchange at the sediment-water interface in rivers involves an analytical solution that combines Darcy's Law and the continuity equation to illustrate the first-order conditions required for infiltration and exfiltration of flow between a stream and its undulating bed. The extent and magnitude of infiltration and exfiltration may be calculated at any distance over the length of a streambed profile whose bed slope, bedform amplitude and wavelength may be specified from field measurements and whose hydraulic gradient varies as a function of discharge. We consider the spatial patterns of exchange for the case where the water surface is essentially planar and the case where it has local curvature as it flows longitudinally over regular sinusoidal bedforms. While some studies refer to bedform-driven exchange when discussing the effect of dynamic head variations determined in part by surface flow separation downstream of bedforms [*Elliott and Brooks*, 1997b], the term "bedform" is used herein to describe streambed topographic features without specification to their size or grain size composition and without reference to effects from dynamic head variations specifically.

This simple theoretical model focuses on the most important features of streambed exchange in lowland gravel bedforms and can be used to provide analytical approximations of the proportion of the bed over which infiltration and exfiltration is possible. A bedform-infiltration relation, which is based on the analytical solution and underlying governing equations, is presented that allows us to quantitatively assess infiltration and exfiltration along irregular or sinusoidal bed profiles. Our interest is in understanding and predicting the patterns of infiltration along the length of lowland gravel bed rivers for the case where (1) the bedform

amplitude is the same order of magnitude as the flow depth itself, and (2) the bedforms are stationary. Some studies have shown that alternating bars can be characterized by a complex distribution of static and dynamic pressure heads that vary in space [*Tonina and Buffington*, 2011], while others have shown that the hydrostatic pressure provides a reasonable approximation of the near-bed pressure distribution for low amplitude bars and bedforms [*Boano et al*., 2014; *Tonina and Buffington*, 2007]. Here, the analytical solution assumes the absence of strong horizontal variations in K and that the dynamic head fluctuations at the sediment-water interface are negligible. We ignored dynamic pressure for this first-order treatment analysis because of our basic intuition from sediment transport (for which purpose the first experiments by *Vittal et al*. [1977] were made) that for lowland gravel-bed rivers, the basic scaling of terms in Equation (1) of *Thibodeaux and Boyle* [1987] indicates that the dynamic pressure gradient term was negligible compared to the hydraulic gradient term (the water-surface slope). However, if we formally follow the lead of Thibodeaux and Boyle, we see that the dynamic pressure term (Equation (2)) comes out to ~0.00032 to 0.000128 when using the head term h_m in Equation (28) of *Elliott and Brooks* [1997b] divided by half of a wavelength of 40 or 100 m. This pressure gradient is a maximum because it assumes flow separation downstream of dune forms, whereas we do not tend to have flow separation downstream of our gradually sloping lee faces of the gravel bars. In the current context, the simple theoretical analysis applies to a longitudinal two-dimensional bed profile that can be regular or irregular, but could be adapted to three-dimensional bed topography. Characterizing the bed by a two-dimensional profile is not meant to claim that the morphology is fully represented by the longitudinal profile; rather, we use it only to gain some mechanistic understanding that can result in better predictions.

Following the theoretical investigation, we conduct a series of two-dimensional numerical simulations of real river bed profiles to examine the effects of observed gravel bed morphology and hydraulic conductivity on the magnitude, extent, and residence time of hyporheic flow along two riffle-pool reaches in the San Joaquin River, CA USA. The 2D numerical groundwater model (Hydrus2D) [*Simunek et al*., 1999] numerically solves the groundwater flow equation for steady, saturated flow, given specifications of the bed topography, water surface gradient, K field and porosity. To define the boundary conditions in the 2D groundwater model, we obtained spatially distributed predictions of water surface elevation, flow depth and velocity based on a set of prior model simulations using the Sedimentation and River Hydraulics Two-dimensional (SRH-2D) [*U.S. Bureau of Reclamation*, 2008] computational model, developed by the U.S. Bureau of Reclamation (USBR). Dynamic pressure head variations over the length of the barform features are included in the numerical modeling, calculated following *Elliott and Brooks* [1997b] based on the pressure data from *Fehlman* [1985], and applied to the observed bed profiles. We pay detailed attention to the changes in the extent and magnitude of the streambed flux resulting from gravel bed morphology and observed heterogeneity in hydraulic conductivity because these features can be specified directly from our field measurements and because some results of general importance emerge.

2. Theory

The flow of water within a streambed is described by Darcy's Law

$$v = -K\frac{dh}{dx} \tag{1}$$

where v is flow velocity, K is the saturated hydraulic conductivity, and dh/dx is the water surface slope. Intragravel flow within a streambed of unit width follows the continuity equation

$$q = Av \tag{2}$$

where q is the flow per unit width and A is the cross-sectional area per unit width of the streambed aquifer (i.e., the thickness per unit width), and v is the Darcian flow velocity.

Vaux [1962] specified that interchange, or exchange I, is the flow rate of stream water entering or exiting the streambed per unit area of the streambed surface. The infiltrating flow is equal to the rate of change of subsurface flow into the streambed. Vaux considered the mass balance in the direction parallel to a planar bed with a step. In contrast, we are considering flow over a low gradient streambed to be essentially horizontal and exchange (infiltration or exfiltration) may be expressed as

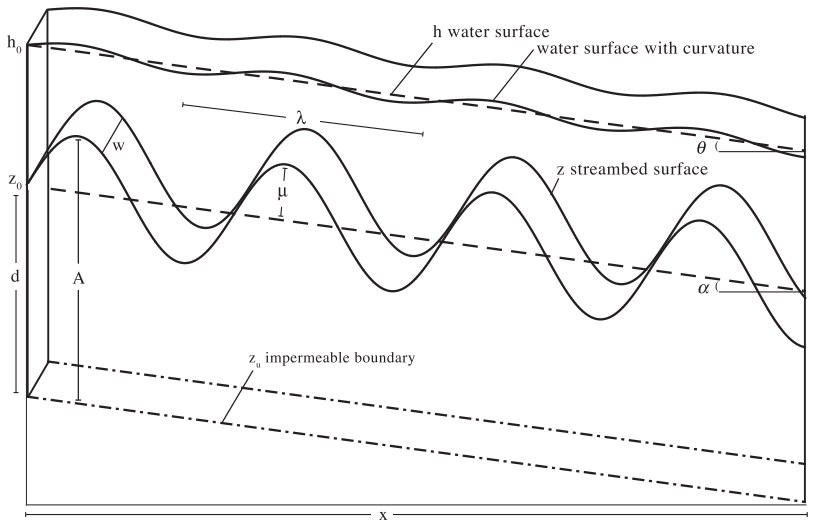

Figure 1. Conceptual diagram of an idealized sloping sinusoidal riverbed underlain by an aquifer of a given thickness and a lower impermeable boundary.

$$I = \frac{dq}{dx} \tag{3}$$

Application of the Dupuit approximation of Darcy's Law to (2) and (3) for a homogenous aquifer yields

$$I = \frac{d(Av)}{dx} = -K\left(\frac{d\left(A \cdot \frac{dh}{dx}\right)}{dx}\right) \tag{4}$$

where h is the water-surface elevation, the total hydraulic head driving flow through the bedform. In the presence of bedforms, $A(x)$, and differentiating gives us

$$I = -K \cdot \left\{\left[\frac{dh}{dx} \cdot \frac{dA}{dx}\right] + \left[A \cdot \frac{d^2h}{dx^2}\right]\right\} \tag{5}$$

where dh/dx is the average water surface gradient (negative in the streamwise direction) and d^2h/dx^2 is the curvature of the water surface. Our differentiation in Equation (5) reflects the fact that, in the presence of an undulating bed surface, the cross-sectional area of the bed aquifer, A, varies with x. We note that Equation (5) does not explicitly account for the bed slope.

We express the elevation of an idealized bed surface z with a sloping sinusoid (Figure 1) as

$$z = z_0 + x\tan\alpha + \frac{\mu}{\cos\alpha} \cdot \sin\left(\frac{2\pi x}{\lambda\cos\alpha}\right) \tag{6}$$

where z is the bed elevation at distance x, z_0 is the elevation of the bed surface at $x = 0$, $\tan\alpha$ is the average gradient of the channel bed (negative in the streamwise direction), which must be equal to the water surface gradient over distances on the order of the reach length in order to retain the flow within the channel, μ is the amplitude of the sinusoidal topography, and λ is the wavelength of the sinusoidal topography. Thus

$$\frac{dz}{dx} = \tan\alpha + \frac{\mu}{\cos\alpha} \cdot \cos\left(\frac{2\pi x}{\lambda\cos\alpha}\right) \cdot \left(\frac{2\pi}{\lambda\cos\alpha}\right) \tag{7}$$

and

$$\frac{d^2z}{dx^2} = -\frac{\mu}{\cos\alpha} \cdot \sin\left(\frac{2\pi x}{\lambda\cos\alpha}\right) \cdot \left(\frac{2\pi}{\lambda\cos\alpha}\right)^2 \tag{8}$$

The elevation of the impermeable boundary at the base of the aquifer beneath the stream can be defined as

$$z_u = (z_0 - d + x\tan\alpha) \tag{9}$$

where d is the thickness of the porous bed below the upstream bed elevation z_0 and is assumed to be constant. The cross-sectional area A of the aquifer per unit width w is

$$A = z - z_u = z_0 + x\tan\alpha + \frac{\mu}{\cos\alpha}\cdot\sin\left(\frac{2\pi x}{\lambda\cos\alpha}\right) - (z_0 - d + x\tan\alpha)$$

which simplifies to

$$A = \frac{\mu}{\cos\alpha}\cdot\sin\left(\frac{2\pi x}{\lambda\cos\alpha}\right) + d. \tag{10}$$

In order to consider infiltration and exfiltration I in the presence of bedforms, we substitute A in Equation (10) into Equation (5) and differentiate to define flow into and out of a sloping sinusoidal bed of a given cross-sectional area:

$$I = -K\cdot\left\{\begin{array}{c}\left[\frac{dh}{dx}\cdot\frac{\mu}{\cos\alpha}\cdot\cos\left(\frac{2\pi x}{\lambda\cos\alpha}\right)\cdot\left(\frac{2\pi}{\lambda\cos\alpha}\right)\right] + \\ \left[\left(\frac{\mu}{\cos\alpha}\cdot\sin\left(\frac{2\pi x}{\lambda\cos\alpha}\right) + d\right)\cdot\frac{d^2h}{dx^2}\right]\end{array}\right\} \tag{11}$$

The bedform-infiltration relation (Equation (11)) indicates that the rate of change of Darcian flow through a sloping sinusoidal bed takes place by two principal mechanisms: (1) topographically-driven flow induced by the interaction of the average head gradient and the bed topography and the spatial variations of the streambed area (shown by the first term in square brackets on the right-hand side of Equation (11)), and (2) water surface curvature-driven flow induced by the combined waviness of the water surface and bed surface (shown by the second term in square brackets on the right-hand side of Equation (11)).

The water-surface curvature is most strongly controlled by the bedform topography when the flow just overtops the riffles and it is least affected when the flow is deep enough to "wash out" their influence and the water surface is more or less planar near bankfull flow (Figure 1). Thus, in lowland gravel bed rivers, the water surface curvature d^2h/dx^2 is likely to be an order of magnitude smaller than the bedform curvature d^2z/dx^2, and it is likely to be smaller during high flows (i.e., when pertubations in the water surface are drowned out) and greater during low flows when the bedforms perturb the velocity field more intensively. To capture this inverse relationship between flow depth and the curvature of the water surface, we let C be represented by the magnitude of the average water-surface gradient in our study reach, which was 0.001 at the highest flow and 0.003 at the lowest flow (Supporting Information (SI) Table S1):

$$\frac{d^2h}{dx^2} \cong C\cdot\frac{d^2z}{dx^2}. \tag{12}$$

Here we are simply trying to obtain a scale for the magnitude of the water-surface curvature, based on field experience from lowland gravel-bed rivers.

When we analyze our field data, a conclusion is that the second term in square brackets on the right-hand side of Equation (11) can be negligible for rivers like those of our study area (Table S1). In similar cases where the water surface curvature is negligible, the second term in square brackets on the right-hand side of Equation (11) goes to zero and Equation (11) can be reduced to:

$$I = -K\cdot\left\{\left[\frac{dh}{dx}\cdot\frac{\mu}{\cos\alpha}\cdot\cos\left(\frac{2\pi x}{\lambda\cos\alpha}\right)\cdot\left(\frac{2\pi}{\lambda\cos\alpha}\right)\right]\right\} \tag{13}$$

The simplified form of Equation (11) (in the absence of strong water surface curvature) indicates that the mechanism driving infiltration is induced by the interaction of the average head gradient and the bed topography (shown by the first term in square brackets on the right-hand side of Equation (11)). However, it is not immediately apparent where the terms for the bed topography (z) or the gradient of the bed topography (dz/dx) appear in the current form of Equation (13).

Recall Equation (7) defines dz/dx. When we rearrange Equation (7) as

$$\frac{dz}{dx} - \tan\alpha = \frac{\mu}{\cos\alpha} \cdot \cos\left(\frac{2\pi x}{\lambda\cos\alpha}\right) \cdot \left(\frac{2\pi}{\lambda\cos\alpha}\right) \tag{14}$$

the left-hand term $(dz/dx - \tan\alpha)$ may be substituted into Equation (12) as follows:

$$I = -K \cdot \frac{dh}{dx} \cdot \left(\frac{dz}{dx} - \tan\alpha\right) \tag{15}$$

We pay attention to the sign of the terms in Equation (15): $-K$ is a negative term and dh/dx is a negative term, so together these two terms are always positive. In contrast, the sign of $(dz/dx - \tan\alpha)$ varies between positive or negative. Therefore, the sign of I depends upon, and is the same as, the sign of $(dz/dx - \tan\alpha)$.

If we assume that (1) at the reach scale, the angle of the average bed slope, α, is the same as the angle of the average water surface, θ, and the slope of aquifer bottom (dz_u/dx), and since we know that (2) $\tan\alpha$ is equal to dh/dx, then Equation (15) can be re-written as

$$I = -K \cdot \frac{dh}{dx} \cdot \left(\frac{dz}{dx} - \frac{dh}{dx}\right) \tag{16}$$

From Equation (16) it is shown that

$$I > 0 \text{ is the same as } \left[-K \cdot \frac{dh}{dx} \cdot \left(\frac{dz}{dx} - \frac{dh}{dx}\right)\right] > 0 \tag{17}$$

Because the term $(-K \cdot dh/dx)$ is a net positive term, the right term in Equation (17) reduces to

$$I > 0 \text{ is the same as } \left(\frac{dz}{dx} - \frac{dh}{dx}\right) > 0 \tag{18}$$

which can be re-arranged to define a final bedform-infiltration relation as:

$$I > 0 \text{ when } \frac{dh}{dx} < \frac{dz}{dx} \text{ (Infiltration)}$$

$$I < 0 \text{ when } \frac{dh}{dx} > \frac{dz}{dx} \text{ (Exfiltration)} \tag{19}$$

Thus, one can simply calculate where along the length of a riverbed I is positive (and where I is negative) by solving for the above inequalities in Equation (19). Infiltration occurs where *dh/dx is more negative than dz/dx*, and exfiltration occurs where *dh/dx is greater than dz/dx*. As defined in Equation (5), dh/dx is a constant negative quantity; therefore infiltration is increasing where A is increasing (i.e., where the bed is rising so dz/dx is less negative than dh/dx). The area over which the bed is rising—and thus where streambed thickness is increasing—is where dz/dx is positive and can be computed directly from Equation (7).

The advantage of the bedform-infiltration relation in Equation (11) is that it can be used to plainly calculate where infiltration can occur along any regular or irregular bed topography with a water surface gradient that varies and has curvature. While the bedform-infiltration relation presented in Equation (19) may not be applicable to small-scale bedforms or in the presence of strong water surface curvature, its utility is that it allows one to simply approximate the *location* and *extent* of streambed infiltration and exfiltration for conditions like those considered here. In the case of negligible water surface curvature, a constant value for dh/dx can be used; subsequent results obtained following Equation (11) will then be identical to those of Equation (19) because the second term on the right-hand side of Equation (11) goes to zero.

3. Methods

The present analysis uses field measurements that were taken along a 2-km reach of the San Joaquin River, beginning at River Mile 259.4 approximately 13.2 km downstream of Friant Dam, near Fresno, California,

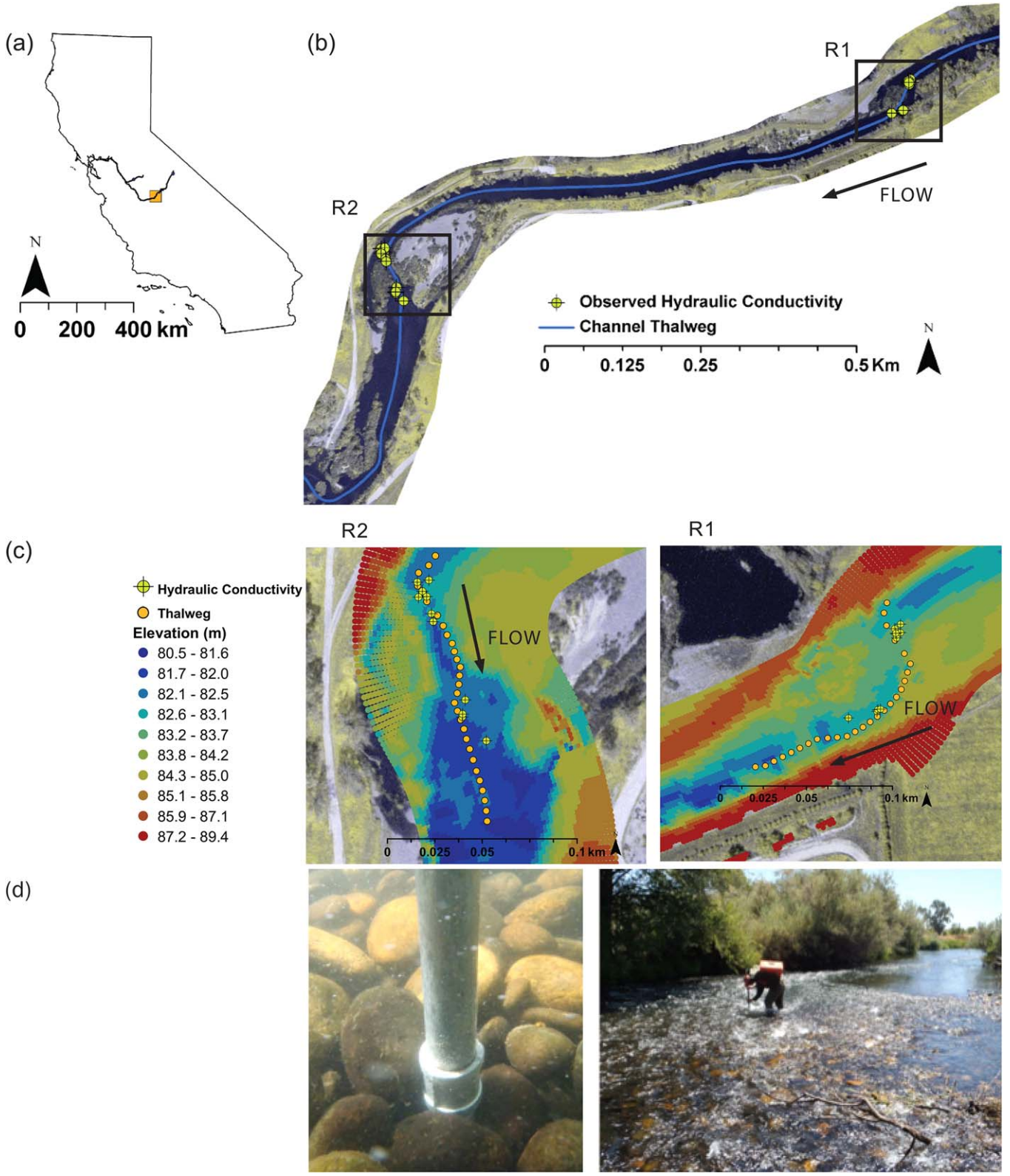

Figure 2. (a) Location of the 2 km study area located approximately 13 km downstream of Friant Dam on the San Joaquin River near Fresno, CA, USA. (b) Detailed aerial map of the 2 km study reach and locations of each of two 150 m long riffle-pool reaches. Also indicated are the locations at which point measurements of streambed hydraulic conductivity were taken at a baseflow of 10 $m^3\ s^{-1}$, the line along which elevation was selected to define the longitudinal streambed profile in the subsurface model domain, and the two riffle-pool reaches upon which this study is focused. (c) Detailed riffle-pool terrain, referred to as Riffle 1 (upstream, at right) and Riffle 2 (downstream, at left). Shown below are (d) corresponding photos illustrating sediment grain size at a K measurement location in Riffle 2 (left) and the location of the thalweg with a fully-submerged lateral bar in Riffle 2 (right).

USA (Figure 2). The 2-km study reach is an anabranch of a gravel-bedded channel with low sinuosity bends expressed as riffle-pool sequences. The anabranch has a mean bankfull width of approximately 60 m and a mean bankfull depth of 0.85 m with an average channel gradient of 0.00059. The riffles average 150 m in length and alternate with pools/runs that average 1200–1500 m in length. The average spacing between riffles/pools is roughly 20 channel widths.

Each of the riffle-pool sequences (referred to as Riffle 1 and Riffle 2 in Figure 2b) consists of a deep pool upstream of a low-amplitude bend that widens and shoals to an oblique riffle crest and lateral bar. Opposite the bar is a narrow, deep scour hole (pool) coinciding with the apex of the bend that shoals to a second elongated midchannel bar. The bars are the eroded remnants of the channel morphology established by the predam flow regime and gravel supply. Riffles throughout this reach have been referred to as "riffle clusters" owing to the occurrence of widely separated pairs of bars.

Field surveys using the Wolman pebble count method and bulk samples [*California Department of Water Resources*, 2010; *U.S. Bureau of Reclamation*, 2014a] in Riffle 1 indicate that the surface is composed of cobbles and coarse gravel, with a median particle size of 64 mm with 84% finer than 80 mm, and 90% finer than 83 mm. In Riffle 2, the surface has a median particle size of 82 mm with 84% finer than 114 mm, and 90% finer than 119 mm. The percent gravel ranges from ∼70–95 percent throughout the 2-km study reach, while the remaining fraction is comprised mostly of sand.

3.1. Field Investigation

3.1.1. Hydraulic Conductivity

Saturated hydraulic conductivity was measured *in situ* with a backpack permeameter and a modified Mark VI Groundwater Standpipe using constant head methods of *Terhune* [1958]. The permeameter measurements were taken during a constant streamflow of 10 $m^3\ s^{-1}$ at 22 sites distributed over the length of two riffle-pool reaches (Figure 2b). At each site, five to eighteen replicate measurements were taken and the average value was calculated. The measurements were taken after a regulated pulse flow of 20 $m^3\ s^{-1}$ during which we observed local mobility of sand and gravel.

The modified groundwater standpipe consisted of a 64-cm length of steel pipe (2.5 cm inner diameter, 3.2 cm outer diameter) tipped with a steel drive point and driven into the streambed with a drive cap and slide hammer. This installation method minimized disturbance to the sediment surrounding the piezometer while measuring the hydraulic conductivity. The lower 5 cm immediately above the drive point is perforated with evenly spaced rows of 3.2 mm diameter holes screened with stainless steel gauze and secured in place by a perforated external steel casing to minimize blockage by fine sediment. Piezometers penetrated the bed to a constant depth of 61 cm, with a midscreen depth located approximately 46 cm below the streambed surface. This depth was selected due to its ecological relevance for salmon spawning [*Crisp and Carling*, 1989; *DeVries*, 1997; *Montgomery et al*., 1996]. Due to difficulty of further advancing a standpipe of relatively large diameter into a tightly compacted and armored bed, K was measured at a single depth at each sampling location.

Calibration results of subsequent experiments by *Barnard and McBain* [1994] demonstrated that the existing Terhune calibration curve is applicable and future calibration is unnecessary if the standpipe perforations are prepared according to similar design. The hydraulic conductivity values were standardized to a water temperature of 10°C based on a viscosity correction factor of 0.9 following Figure 6 in *Barnard and McBain* [1994]. The locations of hydraulic conductivity measurements are shown in Figures 2b and 2c and illustrated with photographs in Figure 2d.

3.1.2. Terrain and Water Surface

We used a two-dimensional hydraulic model to obtain spatially-distributed predictions of water surface elevation for a model of the hyporheic flow field. A two-dimensional hydraulic model of Reach 1a was originally developed and validated for the San Joaquin River (SJR) "Reach 1a" between Friant Dam and Gravelly Ford by the U.S. Bureau of Reclamation and used herein for select steady state flow simulations. A digital terrain model was used to define the elevation of the streambed for each of the two riffle-pool reaches using 2007–2008 photogrammetry, and bathymetry by CDWR and Tetra Tech (USBOR, personal communication, 2013).

Hydraulic model runs were performed using the validated SRH-2D model for each of three experimental discharges used in our simulations: 4.5 $m^3\ s^{-1}$, 10 $m^3\ s^{-1}$, and 20 $m^3\ s^{-1}$. Spatially-explicit values were

obtained for water surface elevation, depth, and velocity along the length of the reach. We extracted the values of the bed and water surface elevation along the thalweg to define the model domain and boundary conditions at the sediment-water interface for the groundwater model. Values of velocity were used in calculation of the dynamic pressure head. Because the 2D flow model provides only the hydrostatic head, dynamic pressure head variations over the length of the barform features were calculated following *Elliott and Brooks* [1997b] based on the pressure data from *Fehlman* [1985], and applied to the boundary conditions over the length of the observed bed profiles. For additional detail regarding the SRH-2D model for the study reach, including the boundary conditions, spatial resolution, and validation, the interested reader is referred to *U.S. Bureau of Reclamation* [2008, 2014b].

3.2. Analytical Investigation

We used the analytical solution for bedform infiltration in Equation (11), and the bedform-infiltration relation presented in Equation (19), together with realistic values for slope, amplitude, wavelength, and hydraulic conductivity informed by our field measurements within the 2-km study reach to quantitatively understand the position and extent of infiltration characteristic of lowland river gravel bars.

Four different idealized morphologies were evaluated: (1) a sinusoidal bed with $\mu = 0.4$ m, $\lambda = 40$ m and $\tan\alpha = -0.005$; (2) a sinusoidal bed with $\mu = 1$ m, $\lambda = 50$ m and $\tan\alpha = -0.005$; (3) an asymmetric bed with bedforms composed of a shorter stoss face and longer lee face; and (4) an asymmetric bed with bedforms composed of a longer stoss face and shorter lee face. For the sinusoidal beds, the streamwise slope of the water surface $\tan\theta$ is assumed to be equal to the average bed slope $\tan\alpha$ and is negative in the downstream direction. We compared the magnitude of the forces driving the exchange, and then compared infiltration zones with and without water surface curvature. For a range of bedform wavelengths and amplitudes, the proportion of the bed over which infiltration occurs was then calculated and compared across different bed morphologies.

3.3. Numerical Simulations

We used a two-dimensional numerical model of Darcian flow in the vertical and longitudinal direction to obtain steady-state, spatially-distributed predictions of pressure head, velocity, and flow direction through each pool-riffle sequence (Hydrus2D) [*Simunek et al.*, 1999]. We examined the subsurface response to a series of controls, with particular focus on quantifying the location and extent of infiltration and exfiltration, the residence time distribution, and the flux of groundwater. The 2D model numerically solves the groundwater flow equation for steady, saturated flow, given the boundary conditions defined by the hydrostatic and dynamic variations in pressure head and specifications of K and porosity. A 2D representation was considered adequate for our purposes because the channel curvature and asymmetry in the cross-stream direction are small, and we are concerned mainly with illustrating general patterns of vertical hyporheic exchange in riffle-pool sequences in wide rivers with minor curvature rather than reproducing the details of flow fields at any particular site.

The profiles of the two pool-riffle sequences were discretized into a structured triangular finite element mesh. The numerical domain of each reach is 2 m deep in the vertical (below a line through the highest bar tops), 150 m in the horizontal, with the surface boundary representing the streambed thalweg along the dotted line shown in Figure 2c. The aquifer is composed of fourteen layers. The thickness of each layer is proportional to the bed elevation relative to the elevation maximum at the riffle crest (approximately 14 cm below the elevation maxima in the reach). Because the groundwater model domain is composed of an irregular mesh grid, the 14 layers are thicker where the bed elevation is the highest, and thinner where the bed elevation is lowest. The depth to the lower boundary was estimated due to a lack of measurements of aquifer thickness in the study reach.

The model simulates subsurface flow along the length of a single riffle-pool sequence with one to two bedform wavelengths. The lower aquifer boundary was chosen to be parallel to the average reach water surface for the 10 $m^3\ s^{-1}$ flow event and its position remained constant across simulations. The upstream vertical boundary ($x = 0$) is assigned a constant flux calculated from the water-surface gradient and the transmissivity profile separately for each scenario. The downstream vertical boundary is assigned a gradient boundary condition often used at the sides of the Hydrus transport domain and reflects the slope of the bed. The final surface boundary is the sediment-water interface at the streambed, with pressure head boundary

conditions determined from water depths computed for each of three experimental discharges (4.5 $m^3 s^{-1}$, 10 $m^3 s^{-1}$, and 20 $m^3 s^{-1}$) with the calibrated SRH-2D flow model. Dynamic pressure head variations over the length of the barform features were calculated following *Elliott and Brooks* [1997b] based on the pressure data from *Fehlman* [1985] and applied to the boundary conditions over the length of the observed bed profiles, as was done in previous studies [*Marzadri et al*., 2014] (SI).

Residence time was calculated by tracking of neutrally buoyant particles under steady boundary conditions with the particles originating at the bedform surface and traveling during the simulations of finite duration (2,000 simulated days). The simulation time thus limits how far some of the particles can travel, and the model limits the number of particles that can be tracked per simulation. For each simulation, particles were placed at 2 m intervals along the streambed surface in the model domain, and were tracked at hourly intervals throughout the simulation period. We also calculated mean hyporheic depth as the average vertical extent of all particle flow paths and the mean flow path length as the average horizontal distance between entry and exit points of hyporheic flow paths. The hyporheic depth is defined here and elsewhere [*Tonina and Buffington*, 2011] as the maximum vertical distance traveled by any water particle that originated as surface water during the simulation period. These metrics have emerged within the study of hydrologic exchange between groundwater and surface water, including the hyporheic exchange depths [*Tonina and Buffington*, 2011; *Valett et al*., 1990], and the distribution of residence times, often calculated with tracers [*Haggerty et al*., 2002] or with particle tracking procedures [*Tonina and Buffington*, 2011]. Some particles originating at the streambed surface are not transported during the particle tracking simulations and the program simply records them as not exiting the domain. Residence times of particles less than 0.1 hours were excluded from this analysis because it is small compared to typical streambed residence times. For this reason, reported residence times are conservative estimates because either the model domain (150 m) or simulation time (2,000 days) was not sufficiently long to compute residence times of those particles originating at the streambed. Some particles may remain in motion in the subsurface for longer distance/time than is the scope of the current investigation. Fluxes into the streambed were calculated by summing the fluxes per unit area of streambed contributions from infiltration. While model simulations yield many flow paths through the bedforms, for this study it was useful to constrain the results to only those flow paths originating at the streambed (as opposed to the upstream vertical boundary) in order to focus on the subsurface response to bedforms. We do not include fluxes into or out of the domain through the upstream or downstream vertical boundaries. For each simulated condition, we mapped the extent of infiltration and exfiltration and calculated the length of streambed for which fluxes were positive or negative. Summary statistics for the residence time, mean flow path length and mean hyporheic depth were calculated for each model scenario.

Spatial patterns of hydraulic conductivity were assigned for every model simulation. We initially assumed the subsurface to be uniform and isotropic, followed by simulations of heterogeneous K fields based on the *in situ* measurements, which though highly variable provide a measure of realism. Because the field measurements of K were taken at spatial intervals of tens of meters over the length of two riffles, and were measured at a uniform depth of 46 cm, we first utilized local polynomial regression fitting to interpolate values at the 2 m spatial resolution along the streambed surface boundary. We then constructed three different plausible heterogeneous K fields based on the sparse measurements to illustrate other potential effects of heterogeneity characteristic of lowland gravel bars. Details of the heterogeneous K fields are described below. Altogether, we constructed 16 simulations comprising 8 scenarios for each of two riffles.

Simulations 1 through 3 assumed uniform and isotropic K of three different magnitudes based on the range of our field measurements: 20, 200, and 2,000 m d^{-1}. In these initial simulations, the water surface gradient was held constant corresponding to a discharge of 10 $m^3 s^{-1}$. Next, we employed uniform and isotropic K taken from the middle of the range of our field measurements (2,000 m d^{-1}) to investigate the effects of changes to the discharge. As such, Simulations 4 and 5 used boundary conditions corresponding to a discharge of 4.5 and 20 $m^3 s^{-1}$, respectively.

Next, the field measurements indicated that two spatial trends in the hydraulic conductivity exist despite the high variability of K arising from measurement uncertainties and sedimentology. First, we observed that K along the bed surface can vary both randomly and with a trend, related to the genesis and inter-flood evolution of gravel bars. Second, particle size data at our own site and observations elsewhere indicate a difference between the loose, surface layer and the denser, more fines-rich subsurface, suggesting that K

decreases with increasing depth. However, it is not possible to establish from the sedimentology of our sites, or from vertical K profiles measured in gravelly reaches of the Sacramento River [*Stillwater Sciences*, 2007] whether a monotonic or layered profile of K is more widespread or applicable in particular sites. Simulations 6 through 8 assumed each of three examples of K decay with depth: exponential decay, linear decay, and stepped decay. The exponential decay of K ranged from 2,000 m d^{-1} at the streambed surface to 20 m d^{-1} at the bottom boundary given by $K=k_0 e^{\ln(100)\cdot(1-n/n_0)}$ where k_0 is the K value at the lower impermeable boundary, n_0 is the total number of K layers beneath the streambed surface, and n is a given layer within the streambed profile. In this scenario (Simulation 6), the interpolated field measurements were not used to define the upper streambed horizon. Instead, a single K value taken from the middle of the range of our field measurements was imposed uniformly along the length of the streambed surface boundary, with each underlying layer being uniform along its length and smaller in magnitude than the overlying layer. In contrast, Simulations 7 and 8 both utilized the observed along-stream K values that are interpolated from our field measurements and assigned them to the upper 8 layers of the K domain representing a spatially-variable coarse surface layer. In the linear decay case (Simulation 7), K decays linearly over the lower remaining fraction of the bed profile at a rate of 0.125 times the overlying streambed surface value subtracted from the immediate overlying K value. Thus, each K value along the bottom boundary varies according to the magnitude of their surface value. Last, in the stepped decay case (Simulation 8), the K decreases in a step-wise manner over the lower remaining fraction of the bed to an intermediate and lower value (2 m d^{-1}). Values assigned to the lower boundary were chosen based on average values reported for sandy beds and the lower range of values for finer gravel beds (e.g., Table 1). This stratigraphy aims to represent systematic sorting of a wide distribution of grain sizes at the surface, each of different mobility, underlain by a more homogenous, impacted, and finer grained material that has been immobile over seasonal time scales. The heterogeneous K fields assigned in Simulations 6 through 8 will be illustrated in the results.

4. Results: Theory

An analytical bedform-infiltration relation presented in Equation (19) for sinusoidal or irregular beds (and Equation (11) for sinusoidal beds) indicates that the rate of change of Darcian flow through bedforms takes place by two principal mechanisms: (1) bedform-driven flow induced by the interaction of the head gradient and the bed topography (the first term on the right-hand side in Equation (11)), and (2) water surface curvature-driven flow induced by the linked curvatures of the water and bed surfaces (the second term on the right-hand side in Equation (11)). Figures 3a and 3b show the infiltration flux over distance for sloping sinusoidal beds of two different amplitudes μ and wavelengths λ, with aspect ratios (λ/μ) of 100 and 50, respectively. Overlaid upon the infiltration flux (black line) is the partial contribution to infiltration from Term 1 (red line) and Term 2 (blue line). For lowland gravel bedforms with amplitudes that are the same order of magnitude as the flow depth itself and aspect ratios (wavelength/height of geomorphic features) that are usually 10 or greater [*Boano et al*., 2014; *Church and Rice*, 2009], the dominant mechanism driving infiltration arises from the interaction of the bedform topography and the head gradient represented by Term 1. This is an important result, which helps to provide quantification of the conceptual model proposed in *Buffington and Tonina* [2009]. In contrast, the curvature of the water surface (Term 2) provides a much smaller contribution to infiltration when it is assumed to be some fraction of the bed curvature (Equations (8) and (12)). Here we assume $\tan\theta$ is -0.005, and K is 20 m d^{-1}.

Combining these two terms, Figure 3 shows that, for the conditions studied, water generally only enters a bedform where the local bed gradient (dz/dx) exceeds the water-surface gradient (dh/dx), which occurs over 50% of the sloping sinusoidal bed. The proportion of the bed over which infiltration occurs is shown following Equation (11) in Figures 3c and 3d where dh/dx is more strongly negative than dz/dx, and following Equation (19) in Figures 3e and 3f where I is positive. The first thing we note is that the two requirements for infiltration yield essentially identical solutions. The prediction following the bedform-infiltration relation in Equation (19)—that infiltration occurs where dh/dx is more strongly negative than dz/dx—is consistent with and almost identical to the prediction following the analytical solution derived in Equation (11). In both Figures 3c and 3e, the curvature of the water surface d^2h/dx^2 is ignored to later demonstrate the difference that the curvature imposes on the infiltration patterns (however, one could obtain the water surface curvature empirically from a hydraulic model). The second thing we note is that infiltration can occur only along the stoss face (upstream) of the bedforms where the bed is rising, and thus where the

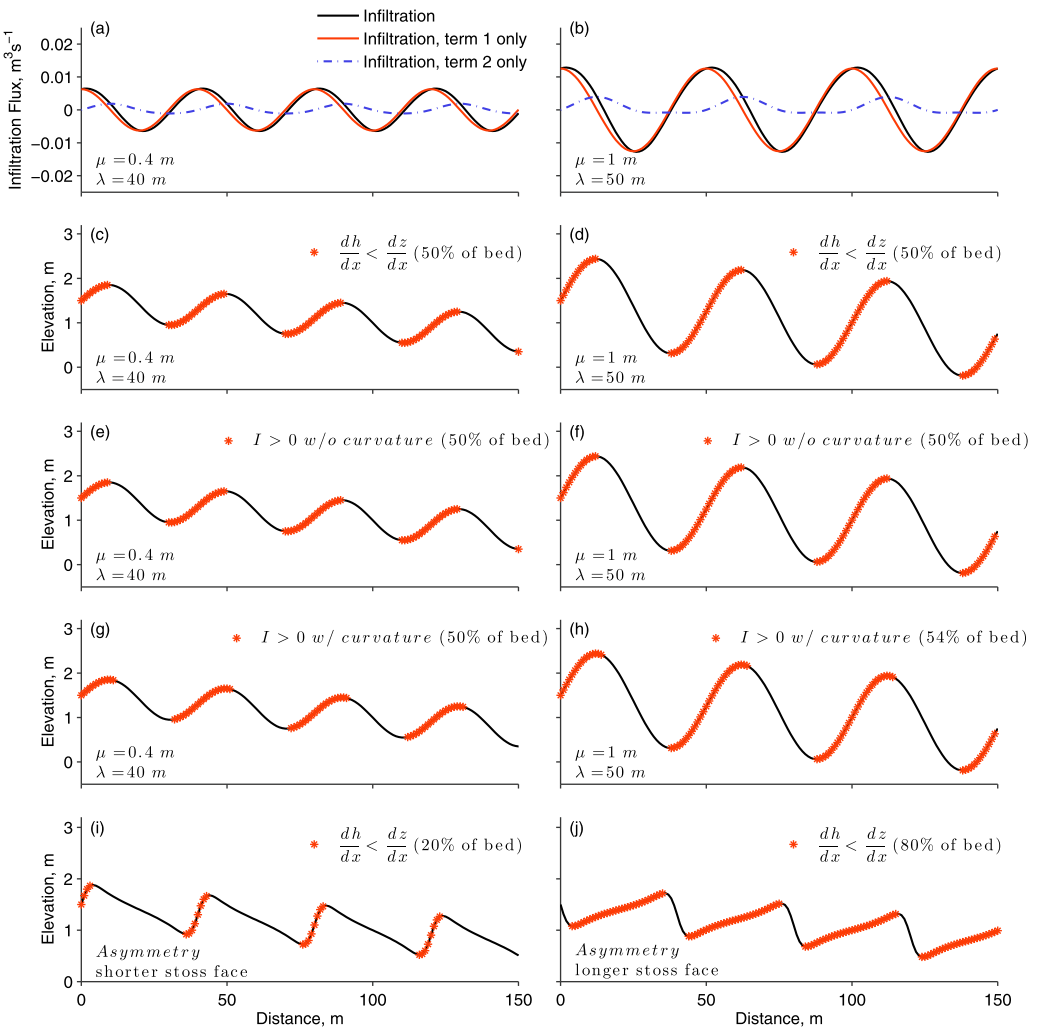

Figure 3. Infiltration along sloping sinusoidal and asymmetric riverbed profiles. A bedform-infiltration relation indicates two mechanisms are convolved: (1) the flow due to the bedform-gradient interaction ("term 1"); (2) the flow due to the water surface curvature ("term 2"). The partial contribution to infiltration from terms 1 (red line) and 2 (blue line) are plotted in Figures 3a and 3b for sloping sinusoidal beds of different amplitudes μ and wavelengths λ while holding K constant (20 m d^{-1}). The net infiltration from both terms is shown by the black line. The corresponding proportion of the bed over which infiltration occurs is shown following Equation (11) in Figures 3c and 3d, and following Equation (19) in Figures 3e and 3f. In Figure 3c through Figure 3f the curvature of the water assumed to be negligible. In contrast, Figures 3g and 3h illustrate the effect of water surface curvature on the extent of infiltration. In Figures 3i and 3j, the bed is asymmetric, drastically reducing the infiltration area to 20% for a bed with a shorter stoss face (Figure 3i) and increasing it to 80% for a bed with longer stoss face (Figure 3j). The sign convention for infiltration in Equation (11) and Equation (19) is positive into the bed ($I > 0$).

streambed thickness (dA/dx) is increasing. Conversely exfiltration occurs on the lee face (downstream) of the bedforms. In the case of purely bedform-driven flow (Figures 3c–3f), flow can only enter the bed from the trough to the bedform crest—but not beyond the crest.

In the presence of water surface curvature (Figures 3g and 3h), some infiltration can occur slightly beyond the peak of the bedform due to the fact that water surface curvature ranges from negative where the topography is convex up to positive where the bed is concave up. Because d^2h/dx^2 is negative over the bedform peaks and remains negative for some distance beyond the crest, it contributes a small amount to infiltration at and slightly downstream of the crest, explaining why the proportion of the bed with infiltration is equal to or slightly greater than that in the absence of curvature. For the bedforms with a greater amplitude and wavelength ($\lambda = 50$m and $\mu = 1$m) only, the water surface curvature causes the proportion of the bed with infiltration to increase from 50% to 54% (Figures 3f and 3h). Conversely, positive values of water surface curvature occur along the pools until reaching the inflection point in the bed topography. In these pool locations, the positive water surface curvature resists infiltration and promotes exfiltration. The

water surface curvature has a negligible effect on the proportion of a bedform reach that accommodates infiltration for the range of lowland bar conditions considered here. The second way that the water surface curvature-dependence might affect the infiltration is through changes in the magnitude of the total infiltration, induced by differences in the total thickness of the porous aquifer *d*, which influences the amount of aquifer area over which the curvature effect on the water surface propagates through the subsurface. Though changes in the aquifer thickness with respect to x occur near the bed surface, the second term on the right-hand side of Equation (11) ("Term 2") indicates that the depth to the impermeable boundary, *d*, is multiplied by the water surface curvature. Thus, the degree to which the water surface curvature has an effect on infiltration depends on the value assigned to *d*, with a deeper impermeable boundary amplifying the curvature-driven effect.

Changes to the amplitude μ or wavelength λ of the sinusoidal bedforms can only alter the extent of infiltration by a few percent despite the fact that such changes can alter the relative magnitude of each of the two contributions to infiltration. This can be seen by comparing the left and right panels in Figure 3. As long as the bedforms are defined by a sinusoidal wave—regardless of changes to μ and λ—the proportion of bed over which infiltration is possible is locked to the topography and the prediction will be that infiltration occurs over approximately 50% of the length of the bed.

If the topography deviates from sinusoidal and instead is composed of irregular or asymmetric bedforms, then the extent over which infiltration is possible is strikingly different (Figures 3i and 3j). Bedform morphology characterized by a short, steep rising stoss face and a longer lee face (Figure 3i) is unfavorable to hyporheic exchange, with infiltration restricted to only ~20% of the bed. In contrast, bedform morphology with a longer stoss face and a shorter lee face (Figure 3j), as is commonly assumed for sandy ripples and dunes, is more favorable to hyporheic exchange with infiltration occurring over ~80% of the bed. The asymmetric topography imposes a first-order control on the proportion of the bed over which infiltration is possible. If the upstream limbs of the bar forms are shorter and steeper than the downstream limbs of the bar forms, then the proportion of the bed available for infiltration is constrained by the topography alone, thereby limiting hyporheic exchange. This is the case at our field site (Tab. S2).

Figure 4 shows the relationship between the proportion of the bed over which infiltration can occur and the bedform aspect ratio (λ/μ). For the range of bedform amplitudes and wavelengths typical of lowland

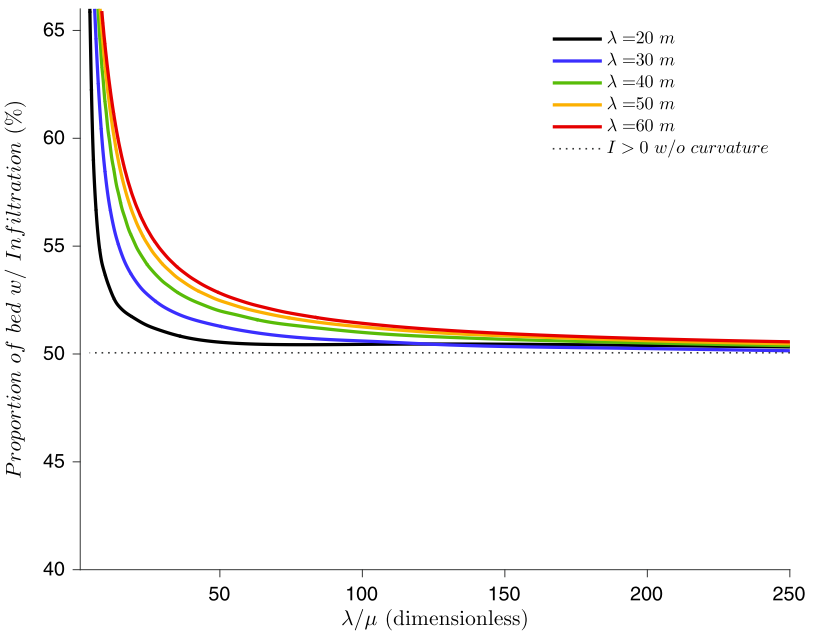

Figure 4. Relationship between the proportion of the bed over which infiltration can occur and the bar wavelength/amplitude. Shown is the infiltration extent along sloping sinusoidal streambeds, reported as a percentage of the bed length for different aspect ratios (wavelength/amplitude of bedforms). Colors denote different values of λ across a range of μ (0.01–5 m). Here we assume a constant slope of –0.005, a constant aquifer depth of 5 m, and uniform K of 20 m d^{-1}.

gravel bed rivers and aspect ratios (wavelength/height of geomorphic features) that are usually 10 or greater [*Boano et al*., 2014; *Church and Rice*, 2009], almost all of the infiltration occurs due to the interaction between the bedform topography and the average water surface gradient (and thus the alluvial thickness) as opposed to the water surface curvature (Figure 3). This can be seen in Figure 4 by comparing the solid lines, which account for water surface curvature, to the dotted line omitting water surface curvature. As values of λ/μ approach the lower range (typical of shorter bedforms such as dunes and ripples) the proportion of the bed with infiltration increases because of the water-surface curvature effect. As the bedform aspect ratio (λ/μ) increases, each of the solid lines converge upon the strictly bedform-driven case where water surface curvature is omitted (dotted line). When values of λ/μ approach 50 or more, the extent of infiltration is locked to and remains near 50% of the bed regardless of the combination of μ and λ, and varies only by a few percent across the different bedform wavelengths. The bedform infiltration relation $dh/dx < dz/dx$, which is nearly equivalent to $I > 0$, captures the relative role of the water surface gradient, topographic gradient, and water surface curvature driving the hyporheic flow into and out of the bed. The case of purely bedform-driven infiltration can be expected to apply for the vast majority of bedform amplitudes and wavelengths in lowland gravel rivers, or when the water surface gradient is constant over the length of a reach and d^2h/dx^2 is small. The bedform-infiltration relation in Equation (19) allows one to easily predict where infiltration is possible along any irregular bed topography simply by calculating the values of dz/dx and dh/dx along each increment of x. Irregularities of the bed topography can be influential enough that infiltration may be limited to only 20% of the bed (Figure 3), whereas that proportion increases to about 50% of the bed in the sloping sinusoid case for the hydrostatic and constant water-surface slope conditions considered here. For real riverbed profiles and a range of discharge, the spatial extent of the inequality in (19) and of the water surface curvature can be defined from the topographic input data and the water surface elevations calculated with a two-dimensional flow model and conveniently mapped in a GIS. Thus, by accounting for bedform asymmetry and calculating the infiltration along the whole channel, it is shown that a significant proportion of infiltration potential at the bed can be lost or gained due to the prevailing barform feature.

5. Results: Field Observations

Discharge and water surface gradient (dh/dx) in the streamwise direction are inversely related (Figure 5a). Model simulations show that the average water surface slope dh/dx along the study reach ranges from -0.001 at high flows (20 cms) and increases to -0.003 at low flows (4.5 cms) (Table S1), with a steeper water surface slope over the length of the riffles at low flow. The vertical exaggeration of topography in Figure 5a makes the streambed surface look rough, but the irregularities along the underlying bar-pool features are only the size of large particles. The inverse relationship of discharge and dh/dx implies that the magnitude of infiltration is greater at low flow than at high flow, though the generality of this result for a three-dimensional case or other two-dimensional cases is not known.

The *in situ* measurements of hydraulic conductivity yielded three interesting observations (Figure 5b): (a) hydraulic conductivity varies by orders of magnitude over the length of a riffle-pool reach, (b) systematic downstream coarsening of the surface layer arises due to the genesis of gravel bars, driven by episodic local bedload transport of gravel that we observed in a minor pulse flow, and (c) sand transported by saltation and suspension during moderate flows and floods permeates the gravel on the crests of riffles while episodic plumes of sand were observed slightly downstream of bar tails.

The K measurements indicate that the observed heterogeneity covaries with topographic features (Figure 5b). Systematic variation over the length of the bar-pool sequences was observed, with the lowest values (< 200 m d^{-1}) measured where the bed slope was positive immediately upstream or at the riffle crest and the highest K values ($> 2{,}000$ m d^{-1}) on the downstream tails of point bars and midchannel bars where the bed slope was negative. Lowest K values were observed in streambed locations close to sites with sieved subsurface bulk surface samples comprising 13–29% sand, though only a few bulk samples coincided with the precise locations of the piezometers. The highest K values ($>12{,}000$ m d^{-1}) were observed at the downstream-most tails of a point bar and a midchannel bar. Though median grain size was not measured at these particular point locations, we observed the sand content to be essentially zero and we documented coarse bedload transport and deposition in narrow zones during a preceding 20 m^3 s^{-1} managed flow

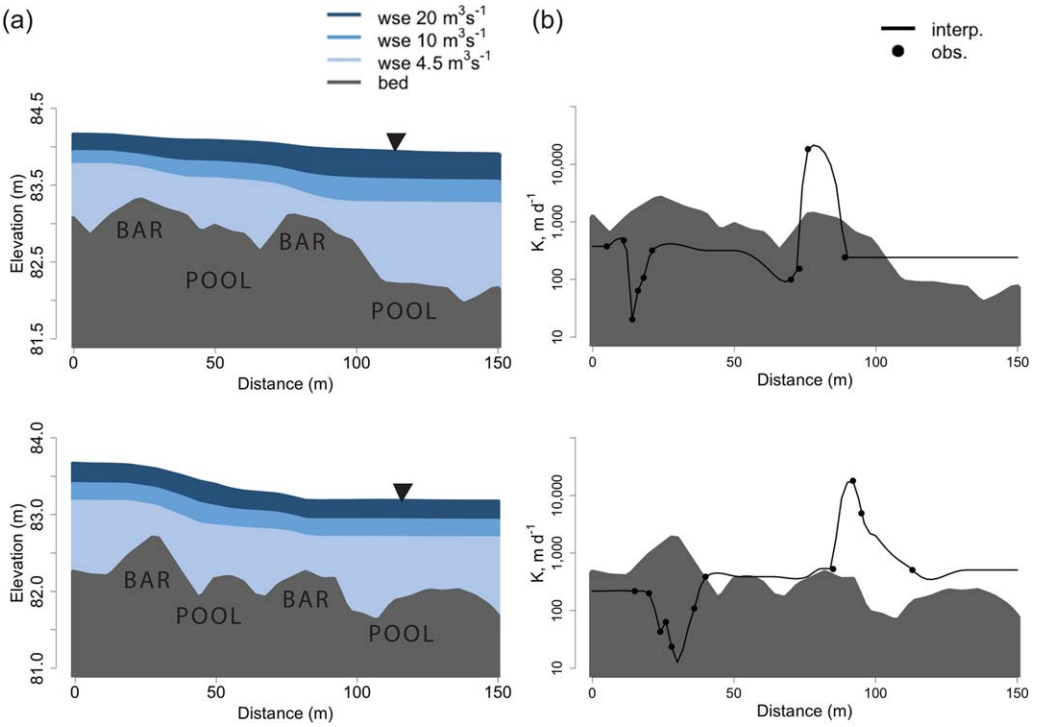

Figure 5. (a) Profile view of riverbed topography and water surface profiles and (b) observed spatial patterns of K, in m d^{-1}, for (top) Riffle 1 and (bottom) Riffle 2.

release. Fitting a single continuous curve through the sparse data points in Figure 5b is not meant to claim that the K field is accurately constrained by the curve, but we use it only to indicate the presence of spatial trends in K that are consistent with the topography, sedimentology, and formation processes of the bars. We assume that much random spatial variability could be superimposed on this pattern with more measurements, but it is not clear how this extra local variability can be measured effectively, given the size of the volume sampled by the equipment for measuring K, or should be interpreted and usefully treated in a simulation model. Our emphasis is on the significance of the barform-scale pattern.

6. Results: Numerical Simulations

The differences in subsurface flow dynamics between the sinusoidal and real riverbed topography observed above alter the overall hydrologic response to given inputs. We can explore the effects of homogenous and heterogeneous K and changes in discharge on hyporheic exchange in two lowland gravel bed reaches of the San Joaquin River, CA, USA by examining in a numerical model (1) the direction, extent and magnitude of streambed fluxes, (2) the subsurface flow fields, and (3) the residence time of the hyporheic flow.

Figure 6 demonstrates that where the total alluvial depth (a maximum of 2 m beneath the bar top) and the bedform wavelength-amplitude ratio is large, and K is uniform, all flow lines roughly parallel the stream surface (Scenarios 1.1–1.3 and 2.1–2.3). However, since water tends to enter the bed where the local bed gradient (*dz/dx*) exceeds the water-surface gradient (*dh/dx*), the asymmetry of the San Joaquin gravel bars and the interaction with the variable water surface elevation can impose a morphologic constraint on infiltration, which is restricted to approximately 45% of the total streambed in the uniform case and as little as 35% of the total streambed in the heterogeneous case (Table 3). Also, the cumulative infiltration flux over 2000 day simulations in Riffle 2 is approximately double that of the less symmetrical Riffle 1 as a result of the different pressure distributions along the streambed. For uniform material under constant discharge (Scenarios 1.1–1.3 and 2.1–2.3), the mean residence time (μ_t) scales inversely and almost linearly with K. The standard deviation of the residence time (σ_t) reflects the variation of the residence time distribution of the linear flow paths through the bedform, and therefore the geometry of the bedforms (Table 2). Likewise, the magnitude of the resulting infiltration fluxes scale positively with K (Table 3).

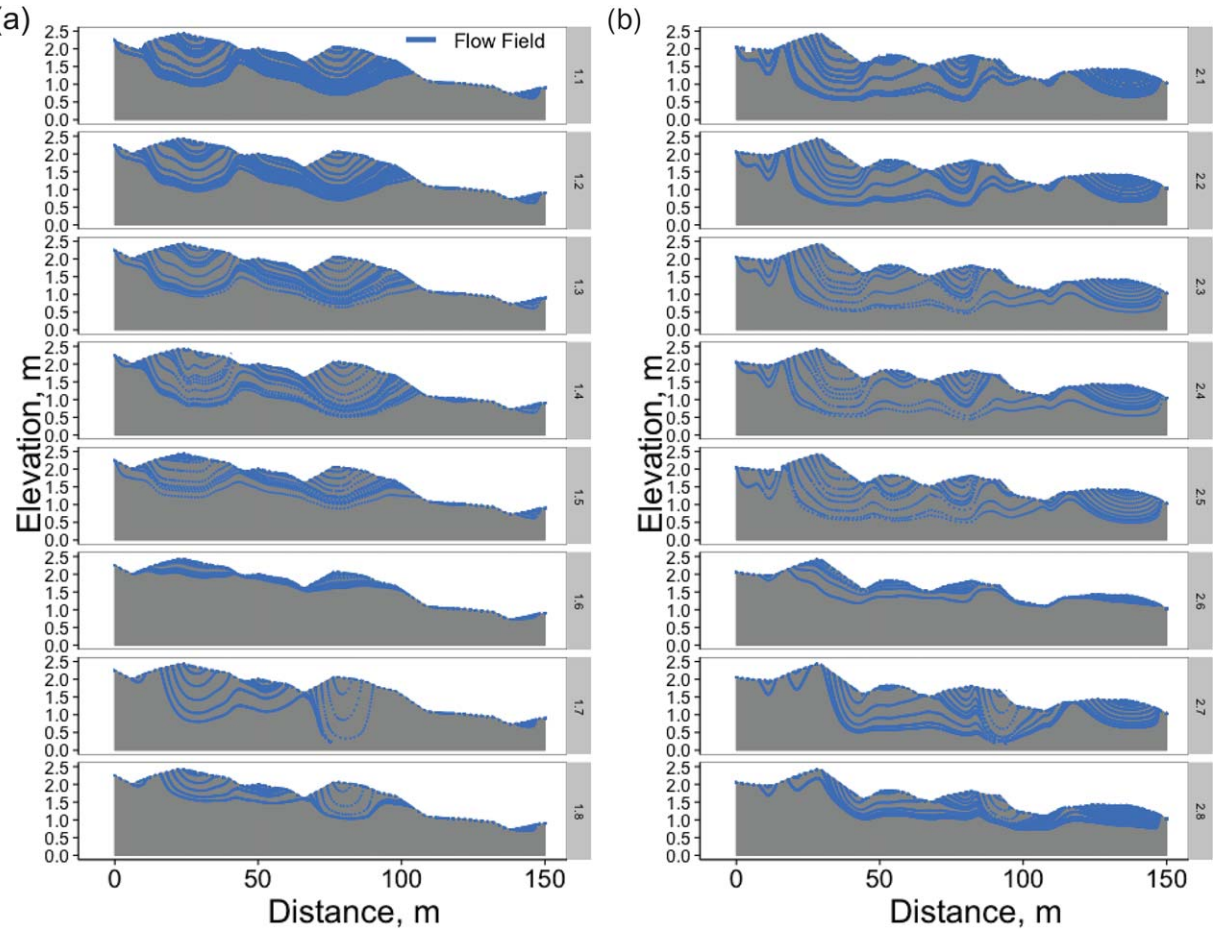

Figure 6. Flowfields illustrating flow path length and depth for all simulations for (a) Riffle 1 and (b) Riffle 2. Summary statistics of flow paths and residence times are reported in Table 2. Numbers shown to the right of each simulation domain (Scenarios 1.1–1.8 and 2.1–2.8) correspond to those model scenarios in Table 2 and 3.

Table 2. Residence Time, Length and Depth of Subsurface Flow Paths for 16 Scenarios in Each of Two Riffle-Pool Sequences[a]

Scenario		River Discharge (m^{-3} s^{-1})	K (m d^{-1})	μ_t (days[b])	ϑ_t (days[b])	σ_t (days[b])	ln_t, (log days[b])	Path Length (x) (m)	Hypor. Depth (z) (m)
Riffle 1									
1.1	Uniform K	10	20	*85.8*	*388.3*	*104.9*	*2.2*	*26.3*	*0.5*
1.2	Uniform K	10	200	*5.7*	*39.0*	*9.4*	*–2.8*	*17.2*	*0.3*
1.3	Uniform K	10	2,000	*0.4*	*4.0*	*0.9*	*–5.4*	*13.3*	*0.3*
1.4	Uniform K	4.5	2,000	*0.4*	*3.7*	*0.8*	*–5.4*	*14.5*	*0.3*
1.5	Uniform K	20	2,000	*0.4*	*4.8*	*1.0*	*–5.7*	*10.5*	*0.2*
1.6	Exponential decay	10	Obs.	*0.5*	*8.1*	*1.4*	*–5.8*	*8.7*	*0.1*
1.7	Linear decay	10	Obs.	*1.2*	*20.1*	*3.2*	*–5.3*	*4.8*	*0.2*
1.8	Stepped decay	10	Obs.	*1.6*	*23.8*	*3.8*	*–5.1*	*6.7*	*0.1*
Riffle 2									
2.1	Uniform K	10	20	*52.7*	*302.5*	*73.3*	*0.7*	*13.5*	*0.4*
2.2	Uniform K	10	200	*4.0*	*31.5*	*6.9*	*–3.3*	*10.2*	*0.3*
2.3	Uniform K	10	2,000	*0.4*	*6.4*	*0.9*	*–5.4*	*9.5*	*0.3*
2.4	Uniform K	4.5	2,000	*0.5*	*6.4*	*1.1*	*–5.4*	*10.0*	*0.3*
2.5	Uniform K	20	2,000	*0.4*	*7.1*	*1.0*	*–5.4*	*10.1*	*0.3*
2.6	Exponential decay	10	Obs.	*0.7*	*18.8*	*2.3*	*–5.6*	*8.0*	*0.1*
2.7	Linear decay	10	Obs.	*2.1*	*17.8*	*3.9*	*–4.2*	*10.8*	*0.3*
2.8	Stepped decay	10	Obs.	*2.9*	*48.9*	*7.8*	*–4.2*	*14.3*	*0.1*

[a]Summary statistics include the mean (μ_t), maximum (ϑ_t), and standard deviation (σ_t) of residence time distributions, the mean of the log of the residence time distributions (ln_t), the mean flow path length, and the mean hyporheic depth.
[b]Summary statistics exclude particles not advectively transported.

Table 3. Cumulative Infiltration Flux at the Streambed, and Length of Streambed for Which Fluxes Were Positive or Negative[a]

Scenario		River Discharge ($m^{-3}s^{-1}$)	K (m d^{-1})	Cumulative Inflow Flux (m^3 d^{-1})	Infiltration Extent (m)	Exfiltration Extent (m)
Riffle 1						
1.1	Uniform K	10	20	−0.57	67	83
1.2	Uniform K	10	200	−5.7	67	83
1.3	Uniform K	10	2,000	−57.2	67	83
1.4	Uniform K	4.5	2,000	−100.9	69	81
1.5	Uniform K	20	2,000	−33.2	61	89
1.6	Exponential decay	10	Obs.	−9.0	60	90
1.7	Linear decay	10	Obs.	−328.2	52	98
1.8	Stepped decay	10	Obs.	−188.0	52	98
Riffle 2						
2.1	Uniform K	10	20	−1.07	61	89
2.2	Uniform K	10	200	−10.7	61	89
2.3	Uniform K	10	2,000	−107.3	61	89
2.4	Uniform K	4.5	2,000	−112.4	63	87
2.5	Uniform K	20	2,000	−114.4	63	87
2.6	Exponential decay	10	Obs.	−18.4	60	80
2.7	Linear decay	10	Obs.	−76.9	64	86
2.8	Stepped decay	10	Obs.	−44.7	64	86

[a]Streambed fluxes are reported per unit width as the actual flux in m^3 d^{-1} per meter streambed length. For all numerical simulations, the sign convention reported is negative for inflow and positive for outflow. Results are summarized for eight model scenarios at each of two riffle-pool sequences.

The degree to which changes in discharge influence the extent and magnitude of infiltration is limited to a few meters and a percentage increase or decrease in the hyporheic flux, respectively. This is shown by comparing the baseflow scenario assuming uniform K of 2,000 m d^{-1} (Table 3, Scenario 1.2 and 2.2) to the scenarios imposing an increase and decrease in discharge (Scenario 1.4, 1.5, 2.4, 2.5). In Figure 6, the flow circulation for both high and low discharge is essentially the same, i.e., all flow lines roughly parallel the stream surface. The total flux into the bed is highest during low flow in Riffle 1, but that is not the case in Riffle 2 (Table 3). Positive and negative spatial velocity gradients at the streambed surface were greatest under low flow conditions corresponding with the steepest water surface slope in Riffle 1 only, a pattern that has been noted elsewhere in the literature [*Boano et al*., 2014]. The fact that the *extent* of infiltration does not change much with discharge relates back to Figure 3 on the theory, because the curvature term (which does interact with the bed topography) is relatively small. The mean residence time μ_t varies only slightly with the water surface slopes corresponding to each discharge (Table 3), whereas the maximum residence times ϑ_t occurred under the highest discharge scenario. However, because lateral water surface gradients were not considered here, it is uncertain whether and how lateral components may influence the results at different discharges.

There is observational [*Powell*, 1998; *Rice and Church*, 2010] and theoretical evidence [*Dietrich*, 1987] from sedimentology and the geomorphology of bar formation to expect substantial spatial variations in hydraulic conductivity across gravel bars and pools. Although it is unlikely that such patterns are going to be measured and incorporated into analyses for most hyporheic zones, it is worth considering what kinds of patterns might occur and their effects on flow in the range of conditions represented in our field study. The first simulation addressing heterogeneity involved exponential decay of K from a spatially uniform value of 2,000 m d^{-1} at the surface to a value of 20 m d^{-1} at the base of the alluvium (Figure 7a). By comparison with the corresponding uniform case (Table 2, Scenario 1.3), exponential decay causes a compression of flow fields to a shallow layer beneath the streambed surface (Figure 6, Scenarios 1.6 and 2.6). However, the μ_t increased by 25% in the case of the upstream bar (Riffle 1) and increased by 75% in the lower bar (Riffle 2). The total infiltration flux along the 150 m length of the bed declined due to the fact that the average K was lower in the exponential-decay case than for the corresponding homogenous case.

For the purposes of illustration, we examined the effects of the along-stream observations of K assuming that the underlying alluvium is approximated by linear decay (Figure 7b). Horizontal variability of K imposes flux divergences and vertical components on the flow field with flow sinking deeper in the most permeable zones on the lee sides of the bars (Figure 6, Scenarios 1.7 and 2.7). The μ_t increased to 1.2 days (σ_t of 3.2

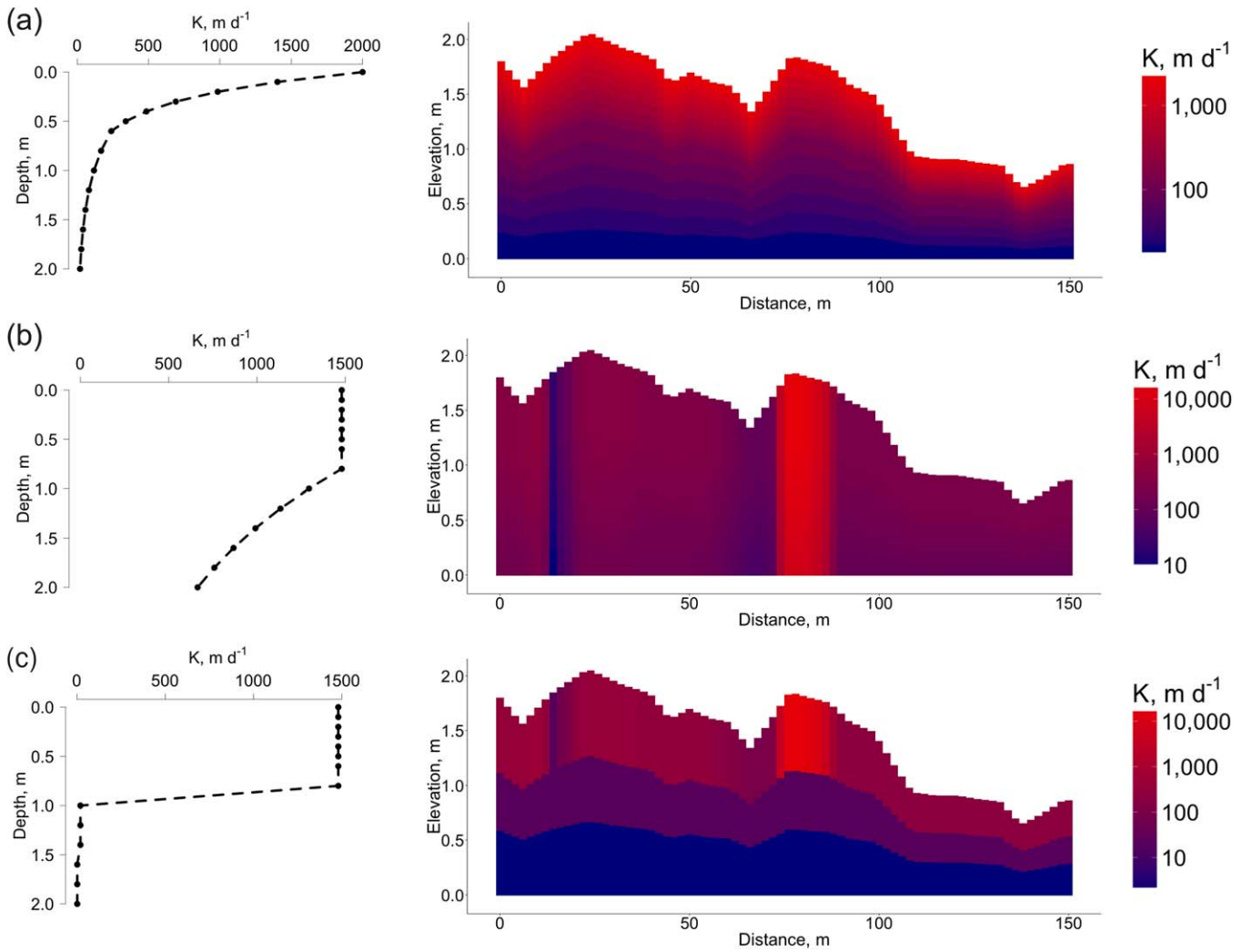

Figure 7. Hydraulic conductivity fields based on direct measurements for three different heterogeneous streambed profiles. Heterogeneous hydraulic conductivity fields correspond to (a) a coarse surface layer with spatially uniform K of 2,000 m d^{-1} that decays exponentially to a value of 20 m d^{-1} at the base of the alluvium (Scenarios 1.6 and 2.6); (b) a spatially heterogeneous surface layer with K that varies every 2 m interpolated linearly between the measured values in Figure 5b, and decays linearly with depth (Scenarios 1.7 and 2.7); and (c) a spatially heterogeneous surface layer with K that varies every 2 m interpolated linearly between the measured values in Figure 5b, and declines with depth in three stepped layers (Scenarios 1.8 and 2.8).

days) in Riffle 1 and 2.1 days (σ_t of 3.9 days) in Riffle 2, and the corresponding total flux into the bed increased in Riffle 1 and decreased in Riffle 2.

In the third examination of potential spatial variations of K, which we believe to reflect the closest representation of K as was measured in the field, the same interpolated along-stream pattern was assigned to the upper 8 layers of the bed, below which K declined abruptly to two low K layers (Figure 7c). Thus, the effects of the surface spatial variability were more strongly confined to the upper 8 layers than in the previous linear-decay case. By comparison with the previous linear case, the hyporheic zone with vertical flow components is constrained to a shallower depth (Figure 6, Scenarios 1.8 and 2.8), therefore the flux is reduced by about one half to one third than in the previous case (Table 3, Scenarios 1.8 and 2.8). The μ_t increases to nearly 1.6 days (σ_t of 3.8 days) from 1.2 days (σ_t of 3.2 days) in the previous scenario (Riffle 1). This increase in μ_t is more pronounced in the more symmetrical Riffle 2, where μ_t increases to nearly 3 days (σ_t of 7.8 days) from 2.1 days (σ_t of 3.9 days) in the previous case. In Riffle 2, the maximum residence time more than doubles due to the addition of slower flow paths. These results agree with those of *Marzadri et al.* [2010] who simulated 3-dimensional hyporheic flow in alternate bars and found that most of the hyporheic flow was confined in a near-bed layer. As a result of the compression of flow paths, they observed residence

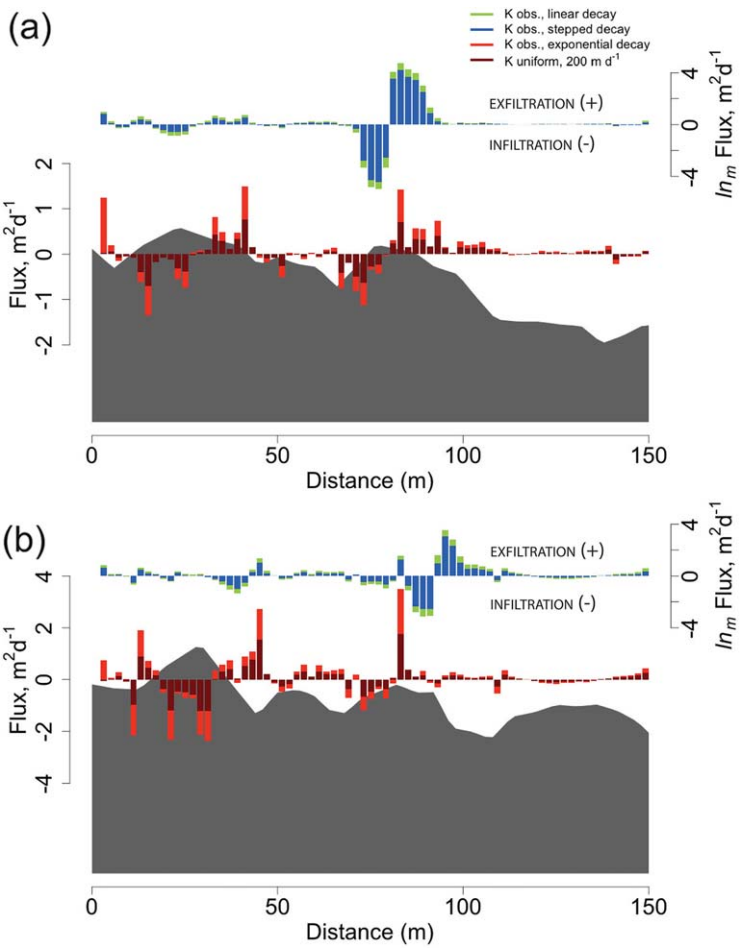

Figure 8. Flux per unit streambed length over the length of each of two riffle-pool sequences. Fluxes are plotted on the left y-axis for uniform medium K (200 m d^{-1}) and one scenario of heterogeneous K assuming exponential decay with depth. Fluxes are plotted on the right *y* axis for two scenarios of heterogeneous K, assuming linear decay with depth, and stepped decay with depth to a uniform low observed K value. A modification of the log transformation (ln_m) was used for plotting flux values corresponding to the right y-axis, in order to spread out the magnitude of the flux data while preserving the sign of data (*SI*). Fluxes are superimposed on the elevation of the streambed; the corresponding axis is omitted, though shown at the same scale as in Figure 5. The sign convention for infiltration in all numerical simulations is negative into the bed.

times to reach a threshold when the alluvial depth is assumed to exceed the channel width, suggesting the assumption of stepped decay in Scenarios 1.8 and 2.8 is physically based.

Asymmetric bedforms considered here have infiltration zones that are considerably shorter than symmetric sinusoidal bedforms (Figure 8 and Table S2), and systematic longitudinal variations in K alone – particularly when low K occurs along the rising bed slope to the riffle crest – can reduce the magnitude of the infiltration flux rates by an order of magnitude or more. In Figure 8, streambed fluxes are plotted on the left y-axis for the uniform medium K (200 m d^{-1}) case and one scenario of heterogeneous K assuming exponential decay with depth. Fluxes are plotted on the right y-axis for two scenarios of heterogeneous K, assuming linear decay and stepped decay. A modification of the log transformation (ln_m) was used for plotting flux values corresponding to the right y-axis, in order to spread out the magnitude of the infiltration and exfiltration flux data while preserving the sign of data following *John and Draper* [1980] (SI). Heterogeneity along the length of the streambed (Scenarios 1.7, 1.8, 2.7, 2.8) generally increased residence time. Flow path length and depth both increased and decreased, and the magnitude of the flux decreased along some infiltration zones, explaining the increase in residence times. For the range of K variations considered in Figure 8, differences in bedform morphology can have a greater influence to the infiltration extent, but changes in K strongly influence the net magnitude of infiltration and throughflow rate at the reach scale. If coarse gravel is clogged by fine sand preferentially along the zones of infiltration, the degree to which the K controls the infiltration flux rate alters the overall hyporheic exchange through the bed. For a given zone of infiltration along the stoss face of the bar, a low K zone reduces the magnitude of the infiltration flux by 1 to 2 orders of magnitude compared to a homogenous bed of gravel. The heterogeneous K pattern provides a mechanistic basis to explain why preferential fining along gravel beds may impose greater resistance to infiltration than coarse gravelly beds or recently mobilized beds. In lowland regulated river environments where there are severe constraints on the supply of coarse sediment and increases in the supply of fine sediment, the preferential reduction of K in zones of infiltration can constrain hyporheic flows to a greater degree than that resulting from low-gradient changes in discharge.

7. Discussion

Perhaps the most important aspect of deriving a simple quantitative relation for quantifying the location and extent of streambed infiltration and exfiltration is that it accounts for distinctly regular properties, namely the bed topography, the hydraulic gradient, the water surface curvature and their interactions. The analytical bedform-infiltration relation presented in Equation (19) and based upon Equation (11) offers several new insights. First, it allows us to formalize a systematic, physically based relation by which to calculate where infiltration and hyporheic exchange can occur. Second, it provides evidence that bedform topography—and especially its asymmetry—is a first-order control on infiltration and hyporheic exchange in low-gradient, low-amplitude bedforms, and that infiltration depends in part on morphogenetic processes via the shaping and thickness of bedforms, the sorting of coarse and fine sediment, and the preferential deposition of fines in the zones where infiltration is possible. Third, it suggests that where bedforms are present in lowland rivers, water surface curvature has only local influence on the infiltration of surface water into and through the subsurface.

The barform features in this study exhibited varying degrees of asymmetry with upstream steeper faces. In the case of sinusoids that others have used as abstract conceptualizations of bedforms, the infiltrating area is locked to around 50% of the bed for any amplitude and wavelength. But many natural bedform fields are asymmetric [e.g., *Carling and Orr*, 2000; *Langbein and Leopold*, 1970] which yields results of the kind we are highlighting here. We have made no attempt herein to analyze the effect of three-dimensional bed topography on the hyporheic flow, which is beyond the scope of the current study. However, it is clear that the three-dimensional nature of the flow field plays a significant role in determining fluxes and residence times for a given set of hydraulic conditions, and could potentially change if the dynamic pressure variations are considered [*Tonina and Buffington*, 2011].

Streambed stratigraphy contains the recent historic record of the formation and maintenance (or migration) of gravel bars, whose hydraulic properties control the location, extent and magnitude of infiltration and exfiltration fluxes, and residence time of intragravel pore water in bar-bend environments. Our own measurements of hydraulic conductivity suggest two fractions of sediment became mobile during a previous pulse flow: a sand fraction and a coarse gravel fraction. Distinguishing the effect of these two fractions upon (1) changes in K over the length of bars and (2) subsequent changes to the hyporheic flux before and after a sediment-mobilizing flood is important in accurate definition of hydraulic characteristics of the streambed.

The results indicate that the effects of heterogeneity on hyporheic flow are fundamentally different depending on whether the topography inherently favors or hinders the area of the bed over which infiltration is possible and whether the low K zones are positioned along zones where infiltration can occur. The K measurements indicate that the observed heterogeneity covaries with topographic features, and that the hydraulic conductivity along the rising bed slope is much lower than that along the declining bed slope. This result emphasizes the importance of controlling sand infiltration, and therefore sand supply, to the spawning habitat of anadromous fish [e.g., *Maturana et al.*, 2014]. Our own simulations did not consider how the variations in K might alter the influence of differences in alluvial thickness. A fuller investigation of this phenomenon and its implications for the extent and magnitude of infiltration and hyporheic flow in lowland gravel bed rivers is left for future work.

Acknowledgments
This work was supported by the Delta Stewardship Council Delta Science Program under Award Number U-04-SC-005. Data used in this article can be obtained from the lead author. E.B. and T.D. contributed equally to designing the analysis, developing the bedform-infiltration relation and numerical model, synthesizing results and writing the manuscript. We acknowledge five anonymous reviewers for their thoughtful comments, which greatly improved the manuscript.

References

Alderdice, D., and F. Velsen (1978), Relation between temperature and incubation time for eggs of chinook salmon (Oncorhynchus tshawytscha), *J. Fish. Board Can.*, *35*(1), 69–75.

Arntzen, E. V., D. R. Geist, and P. E. Dresel (2006), Effects of fluctuating river flow on groundwater/surface water mixing in the hyporheic zone of a regulated, large cobble bed river, *River Res. Appl.*, *22*(8), 937–946.

Bardini, L., F. Boano, M. B. Cardenas, A. H. Sawyer, R. Revelli, and L. Ridolfi (2013), Small-scale permeability heterogeneity has negligible effects on nutrient cycling in streambeds, *Geophys. Res. Lett.*, *40*, 1118–1122, doi:10.1002/grl.50224.

Barnard, K., and S. McBain (1994), Standpipe to determine permeability, dissolved oxygen, and vertical particle size distribution in salmonid spawning gravels, Eureka, California: U.S. Department of Agriculture Forest Service, *Fish Habitat Relationships Tech. Bull. 15*.

Barontini, S., A. Clerici, R. Ranzi, and B. Bacchi (2005), Saturated hydraulic conductivity and water retention relationships for Alpine mountain soils, in *Climate and Hydrology of Mountain Areas*, edited by C. de Jong, D. Collins, and R. Ranzi, pp. 101–121, John Wiley, Hoboken, N. J.

Beacham, T. D., and C. B. Murray (1990), Temperature, egg size, and development of embryos and alevins of five species of Pacific salmon: A comparative analysis, *Trans. Am. Fish. Soc.*, *119*(6), 927–945.

Blom, A., J. S. Ribberink, and H. J. de Vriend (2003), Vertical sorting in bedforms: Flume experiments with a natural and a trimodal sediment mixture, *Water Resour Res*, *39*(2), 1025, doi:10.1029/2001WR001088.

Boano, F., R. Revelli, and L. Ridolfi (2007), Bedform-induced hyporheic exchange with unsteady flows, *Adv Water Resour*, *30*(1), 148–156.
Boano, F., J. W. Harvey, A. Marion, A. I. Packman, R. Revelli, L. Ridolfi, and A. Wörman (2014), Hyporheic flow and transport processes: Mechanisms, models, and biogeochemical implications, *Rev. Geophys.*, *52*, 603–679, doi:10.1002/2012RG000417.
Buffington, J. M., and D. Tonina (2009), Hyporheic exchange in Mountain Rivers II: Effects of channel morphology on mechanics, scales, and rates of exchange, *Geogr. Compass*, *3*(3), 1038–1062.
California Department of Water Resources (2010), CDWR 2009 Interim Flows Data Report DRAFT, 3/26/2010. Appendix IV: 34 San Joaquin River Riffle Particle Size Composition Survey Interim Report, River Miles 247 – 267. Final draft report, Fresno, Calif.
Cardenas, M. B., and V. A. Zlotnik (2003), A simple constant-head injection test for streambed hydraulic conductivity estimation, *Ground Water*, *41*(6), 867–871.
Cardenas, M. B., J. L. Wilson, and V. A. Zlotnik (2004), Impact of heterogeneity, bedforms, and stream curvature on subchannel hyporheic exchange, *Water Resour Res*, *40*, W08307, doi:10.1029/2004WR003008.
Carling, P. A., and H. G. Orr (2000), Morphology of riffle-pool sequences in the River Severn, England, *Earth Surf. Processes Landforms*, *25*(4), 369–384.
Chen, X. (2000), Measurement of streambed hydraulic conductivity and its anisotropy, *Environ. Geol.*, *39*(12), 1317–1324.
Church, M., and S. P. Rice (2009), Form and growth of bars in a wandering gravel-bed river, *Earth Surf. Processes Landforms*, *34*(10), 1422–1432.
Church, M., M. A. Hassan, and J. F. Wolcott (1998), Stabilizing self-organized structures in gravel-bed stream channels: Field and experimental observations, *Water Resour. Res.*, *34*(11), 3169–3179.
Conant, B., J. A. Cherry, and R. W. Gillham (2004), A PCE groundwater plume discharging to a river: Influence of the streambed and near-river zone on contaminant distributions, *J. Contam. Hydrol.*, *73*(1), 249–279.
Crisp, D., and P. Carling (1989), Observations on siting, dimensions and structure of salmonid redds, *J. Fish. Biol.*, *34*(1), 119–134.
DeVries, P. (1997), Riverine salmonid egg burial depths: Review of published data and implications for scour studies, *Can. J. Fish. Aquat. Sci.*, *54*(8), 1685–1698.
Dietrich, W. E. (1987), Mechanics of flow and sediment transport in river bends, in *River Channels Environment and Process*, edited by K. S. Richards, pp. 179–224, Basil Blackwell, Oxford.
Dietrich, W. E., J. W. Kirchner, H. Ikeda, and F. Iseya (1989), Sediment supply and the development of the coarse surface layer in gravel-bedded rivers, *Nature*, *340*(6230), 215–217.
Edwards, R. T. (1998), The hyporheic zone, in *River Ecology and Management: Lessons from the Pacific Coastal Ecoregion*, edited by R. J. Naiman, R. E. Bilby, pp. 339–429, Springer-Verlag: New York.
Elliott, A. H., and N. H. Brooks (1997b), Transfer of nonsorbing solutes to a streambed with bedforms: Theory, *Water Resour. Res.*, *33*(1), 123–136.
Evans, E., and A. Wilcox (2014), Fine sediment infiltration dynamics in a gravel-bed river following a sediment pulse, *River Res. Appl.*, *30*(3), 372–384.
Fehlman, H. M. (1985), Resistance components and velocity distributions of open channel flows over bedforms, M.S. thesis, pp. 338, Colo. State Univ., Fort Collins.
Geist, D. R., and D. D. Dauble (1998), Redd site selection and spawning habitat use by fall chinook salmon: The importance of geomorphic features in large rivers, *Environ. Manage.*, *22*(5), 655–669.
Geist, D. R., C. S. Abernethy, K. D. Hand, V. I. Cullinan, J. A. Chandler, and P. A. Groves (2006), Survival, development, and growth of fall Chinook salmon embryos, alevins, and fry exposed to variable thermal and dissolved oxygen regimes, *Trans. Am. Fish. Soc.*, *135*(6), 1462–1477.
Genereux, D. P., S. Leahy, H. Mitasova, C. D. Kennedy, and D. R. Corbett (2008), Spatial and temporal variability of streambed hydraulic conductivity in West Bear Creek, North Carolina, USA, *J. Hydrol.*, *358*(3), 332–353.
Gomez-Velez, J. D., and J. W. Harvey (2014), A hydrogeomorphic river network model predicts where and why hyporheic exchange is important in large basins, *Geophys. Res. Lett.*, *41*, 6403–6412, doi:10.1002/2014GL061099.
Gomez-Velez, J. D., S. Krause, and J. L. Wilson (2014), Effect of low-permeability layers on spatial patterns of hyporheic exchange and groundwater upwelling, *Water Resour. Res.*, *50*, 5196–5215, doi:10.1002/2013WR015054.
Greig, S., D. Sear, and P. Carling (2005), The impact of fine sediment accumulation on the survival of incubating salmon progeny: Implications for sediment management, *Sci. Total Environ.*, *344*(1), 241–258.
Haggerty, R., S. M. Wondzell, and M. A. Johnson (2002), Power-law residence time distribution in the hyporheic zone of a 2nd-order mountain stream, *Geophys. Res. Lett.*, *29*(13), 1640, doi:10.1029/2002GL014743.
Hanrahan, T. P., D. R. Geist, and E. V. Arntzen (2005), Habitat quality of historic Snake River fall Chinook salmon spawning locations and implications for incubation survival. Part 1: Substrate quality, *River Res. Appl.*, *21*(5), 455–467.
Harvey J. W., and K. E. Bencala (1993), The effect of streambed topography on surface-subsurface water exchange in mountain catchments, *Water Resour. Res.*, *29*(1), 89–98.
Hatch, C. E., A. T. Fisher, C. R. Ruehl, and G. Stemler (2010), Spatial and temporal variations in streambed hydraulic conductivity quantified with time-series thermal methods, *J. Hydrol.*, *389*(3–4), 276–288.
Hester, E., K. Young, and M. Widdowson (2013), Mixing of surface and groundwater induced by riverbed dunes: Implications for hyporheic zone definitions and pollutant reactions, *Water Resour. Res.*, *49*, 5221–5237, doi:10.1002/wrcr.20399.
Ingendahl, D. (2001), Dissolved oxygen concentration and emergence of sea trout fry from natural redds in tributaries of the River Rhine, *J. Fish. Biol.*, *58*(2), 325–341.
John, J., and N. Draper (1980), An alternative family of transformations, *Appl Stat.*, *29*, 190–197.
Kasahara, T., and S. M. Wondzell (2003), Geomorphic controls on hyporheic exchange flow in mountain streams, *Water Resour Res*, *39*(1), 1005, doi:10.1029/2002WR001386.
Kennedy, C. D., D. P. Genereux, D. R. Corbett, and H. Mitasova (2009), Relationships among groundwater age, denitrification, and the coupled groundwater and nitrogen fluxes through a streambed, *Water Resour Res*, *45*, W09402, doi:10.1029/2008WR007400.
Kondolf, G. M. (2000), Assessing salmonid spawning gravel quality, *T Am Fish Soc*, *129*(1), 262–281.
Kondolf, G. M., and P. R. Wilcock (1996), The Flushing flow problem: Defining and evaluating objectives, *Water Resour. Res.*, *32*(8), 2589–2599.
Konrad, C. P., D. B. Booth, S. J. Burges, and D. R. Montgomery (2002), Partial entrainment of gravel bars during floods, *Water Resour. Res.*, *38*(7), 1104, doi:10.1029/2001WR000828.
Landon, M. K., D. L. Rus, and F. E. Harvey (2001), Comparison of instream methods for measuring hydraulic conductivity in sandy streambeds, *Groundwater*, *39*(6), 870–885.
Langbein, W. B., and L. B. Leopold (1970), River meanders and the theory of minimum variance, in *Rivers and river terraces*, pp. 238–263, Palgrave Macmillan, U. K.

Lapointe, M. F., N. E. Bergeron, F. Bérubé, M.-A. Pouliot, and P. Johnston (2004), Interactive effects of substrate sand and silt contents, redd-scale hydraulic gradients, and interstitial velocities on egg-to-emergence survival of Atlantic salmon (Salmo salar), *Can. J. Fish. Aquat. Sci.*, *61*(12), 2271–2277.
Lautz, L. K., and D. I. Siegel (2006), Modeling surface and ground water mixing in the hyporheic zone using MODFLOW and MT3D, *Adv. Water Resour.*, *29*(11), 1618–1633.
Leek, R., J. Q. Wu, L. Wang, T. P. Hanrahan, M. E. Barber, and H. Qiu (2009), Heterogeneous characteristics of streambed saturated hydraulic conductivity of the Touchet River, south eastern Washington, USA, *Hydrol. Processes*, *23*(8), 1236–1246.
Leopold, L. (1992), Sediment size that determines channel morphology, in *Dynamics of Gravel-Bed Rivers*, edited by P. Billi et al., pp. 297–311., John Wiley and Sons Ltd.
Marion, A., A. I. Packman, M. Zaramella, and A. Bottacin-Busolin (2008), Hyporheic flows in stratified beds, *Water Resour Res*, *44*, W09433, doi:10.1029/2007WR006079.
Marzadri, A., D. Tonina, A. Bellin, G. Vignoli, and M. Tubino (2010), Semianalytical analysis of hyporheic flow induced by alternate bars, *Water Resour. Res.*, *46*, W07531, doi:10.1029/2009WR008285.
Marzadri, A., D. Tonina, J. McKean, M. Tiedemann, and R. Benjankar (2014), Multi-scale streambed topographic and discharge effects on hyporheic exchange at the stream network scale in confined streams, *J. Hydrol.*, *519*, 1997–2011.
Maturana, O., D. Tonina, J. A. McKean, J. M. Buffington, C. H. Luce, and D. Caamaño (2014), Modeling the effects of pulsed versus chronic sand inputs on salmonid spawning habitat in a low-gradient gravel-bed river, *Earth Surf. Processes Landforms*, *39*(7), 877–889.
Milne, J. (1982), Bed-material size and the riffle-pool sequence, *Sedimentology*, *29*(2), 267–278.
Montgomery, D. R., J. M. Buffington, N. P. Peterson, D. Schuett-Hames, and T. P. Quinn (1996), Stream-bed scour, egg burial depths, and the influence of salmonid spawning on bed surface mobility and embryo survival, *Can. J. Fish. Aquat. Sci.*, *53*(5), 1061–1070.
Mosley, M. P. (1981), The influence of organic debris on channel morphology and bedload transport in a New Zealand forest stream, *Earth Surf. Processes Landforms*, *6*(6), 571–579.
Packman, A. I., and J. S. MacKay (2003), Interplay of stream-subsurface exchange, clay particle deposition, and streambed evolution, *Water Resour. Res.*, *39*(4), 1097, doi:10.1029/2002WR001432.
Packman, A. I., M. Salehin, and M. Zaramella (2004), Hyporheic exchange with gravel beds: Basic hydrodynamic interactions and bedform-induced advective flows, *J. Hydraul. Eng.*, *130*(7), 647–656.
Packman, A. I., A. Marion, M. Zaramella, C. Chen, J.-F. Gaillard, and D. T. Keane (2006), Development of layered sediment structure and its effects on pore water transport and hyporheic exchange, *Water Air Soil Pollut. Focus*, *6*(5), 433–442.
Parker, G., and A. J. Sutherland (1990), Fluvial armor, *J. Hydraul. Res.*, *28*(5), 529–544.
Powell, D. M. (1998), Patterns and processes of sediment sorting in gravel-bed rivers, *Prog. Phys. Geogr.*, *22*(1), 1–32.
Reid, L. M., and T. Dunne (2003), Sediment budgets as an organizing framework in fluvial geomorphology, in *Tools in Fluvial Geomorphology*, edited by G. M. Kondolf and H. Piegay, pp. 463–500, John Wiley, Chichester, U. K.
Rice, S. P., and M. Church (2010), Grain-size sorting within river bars in relation to downstream fining along a wandering channel, *Sedimentology*, *57*(1), 232–251.
Rosenberry, D. O., and J. Pitlick (2009), Local-scale variability of seepage and hydraulic conductivity in a shallow gravel-bed river, *Hydrol. Processes*, *23*(23), 3306–3318.
Rosenberry, D. O., M. A. Briggs, G. Delin, and D. K. Hare (2016), Combined use of thermal methods and seepage meters to efficiently locate, quantify, and monitor focused groundwater discharge to a sand-bed stream, *Water Resour. Res.*, *52*, 4486–4503, doi:10.1002/2016WR018808.
Ryan, R., and M. Boufadel (2006), Influence of streambed hydraulic conductivity on solute exchange with the hyporheic zone, *Environ. Geol.*, *51*(2), 203–210.
Salehin, M., A. I. Packman, and M. Paradis (2004), Hyporheic exchange with heterogeneous streambeds: Laboratory experiments and modeling, *Water Resour. Res.*, *40*, W11504, doi:10.1029/2003WR002567.
Savant, S. A., D. D. Reible, and L. J. Thibodeaux (1987), Convective transport within stable river sediments, *Water Resour. Res.*, *23*(9), 1763–1768.
Sawyer, A. H., and M. B. Cardenas (2009), Hyporheic flow and residence time distributions in heterogeneous cross-bedded sediment, *Water Resour. Res.*, *45*, W08406, doi:10.1029/2008WR007632.
Shope, C. L., J. E. Constantz, C. A. Cooper, D. M. Reeves, G. Pohll, and W. A. McKay (2012), Influence of a large fluvial island, streambed, and stream bank on surface water-groundwater fluxes and water table dynamics, *Water Resour. Res.*, *48*, W06512, doi:10.1029/2011WR011564.
Simunek, J., M. Sejna, and M. van Genuchten (1999), *The HYDRUS-2D Software Package for Simulating Two-Dimensional Movement of Water, Heat, and Multiple Solutes in Variably-Saturated Media, Version 2.0*, U.S. Salinity Lab., USDA, ARS, Riverside, Calif.
Stewardson, M., T. Datry, N. Lamouroux, H. Pella, N. Thommeret, L. Valette, and S. Grant (2016), Variation in reach-scale hydraulic conductivity of streambeds, *Geomorphology*, *259*, 70–80.
Stillwater Sciences (2007), Sacramento River ecological flows study: TUGS simulation of the Sacramento River between Keswick Dam and Clear Creek, final report, Berkeley, Calif.
Storey, R. G., K. W. Howard, and D. D. Williams (2003), Factors controlling riffle-scale hyporheic exchange flows and their seasonal changes in a gaining stream: A three-dimensional groundwater flow model, *Water Resour. Res.*, *39*(2), 1034, doi:10.1029/2002WR001367.
Suttle, K. B., M. E. Power, J. M. Levine, and C. McNeely (2004), How fine sediment in riverbeds impairs growth and survival of juvenile salmonids, *Ecol. Appl.*, *14*(4), 969–974.
Terhune, L. (1958), The Mark VI groundwater standpipe for measuring seepage through salmon spawning gravel, *J. Fish. Board Can.*, *15*(5), 1027–1063.
Thibodeaux, L. J., and J. D. Boyle (1987), Bedform-generated convective transport in bottom sediment, *Nature*, *325*, 341–343.
Tonina, D., and J. M. Buffington (2007), Hyporheic exchange in gravel bed rivers with pool-riffle morphology: Laboratory experiments and three-dimensional modeling, *Water Resour. Res.*, *43*, W01421, doi:10.1029/2005WR004328.
Tonina, D., and J. M. Buffington (2009b), A three-dimensional model for analyzing the effects of salmon redds on hyporheic exchange and egg pocket habitat, *Can. J. Fish. Aquat. Sci.*, *66*(12), 2157–2173.
Tonina, D., and J. M. Buffington (2009a), Hyporheic exchange in Mountain Rivers I: Mechanics and environmental effects, *Geogr. Compass*, *3*(3), 1063–1086.
Tonina, D., and J. M. Buffington (2011), Effects of stream discharge, alluvial depth and bar amplitude on hyporheic flow in pool-riffle channels, *Water Resour. Res.*, *47*, W08508, doi:10.1029/2010WR009140.
Tonina, D., F. P. de Barros, A. Marzadri, and A. Bellin (2016), Does streambed heterogeneity matter for hyporheic residence time distribution in sand-bedded streams?, *Adv. Water Resour.*, *96*, 120–126.

U.S. Bureau of Reclamation (2008), *SRH-2D Theory and User's Manual Version 2.0*, prepared by Y.G. Lai, Tech. Serv. Cent., Bur. of Reclam., Denver, Colo.
U.S. Bureau of Reclamation (2014a), *SJRRP Sediment Gradation Atlas, 1995–2012*, draft version 2.1, Tech. Serv. Cent., Bur. of Reclam., Denver, Colo.
U.S. Bureau of Reclamation (2014b), Two-Dimensional Modeling of Reach 1A of the San Joaquin River between Friant Dam and Highway 99, *Tech. Rep. SRH-2014–14*, prepared by E. Gordon and B. Greimann, p. 48, U.S. Bur. of Reclam., San Joaquin River Restoration Proj. Mid-Pacific Region, Denver, Colo.
Valett, H. M., S. G. Fisher, and E. H. Stanley (1990), Physical and Chemical Characteristics of the Hyporheic Zone of a Sonoran Desert Stream, *J. North Am. Benthol. Soc.*, *9*(3), 201–215.
Vaux, W. G. (1962), *Interchange of Stream and Intragravel Water in a Salmon Spawning Riffle*, Spec. Sci. Rep., 11 pp., US Fish and Wildl. Serv., Bur. of Commercial Fish., Washington, D. C.
Vittal, N., K. Ranga Raju, and R. Garde (1977), Resistance of two dimensional triangular roughness, *J. Hydraul. Res.*, *15*(1), 19–36.
Wang, L., J. Song, B. Zhang, H. Guo, W. Jiang, M. Wen, and G. Zhang (2016), Spatial and temporal variations of streambed vertical hydraulic conductivity in the Weihe River, China, *Water*, *8*(3), 70.
Wickett, W. P. (1954), The oxygen supply to salmon eggs in spawning beds, *J. Fish. Board Can.*, *11*(6), 933–953.
Wilcock, P. R., and B. T. DeTemple (2005), Persistence of armor layers in gravel-bed streams, *Geophys Res. Lett.*, *32*, L08402, doi:10.1029/2004GL021772.
Yager, E. M., J. W. Kirchner, and W. E. Dietrich (2007), Calculating bed load transport in steep boulder bed channels, *Water Resour. Res.*, *43*, W07418, doi:10.1029/2006WR005432.
Zlotnik, V. A., M. B. Cardenas, and D. Toundykov (2011), Effects of multiscale anisotropy on basin and hyporheic groundwater flow, *Ground Water*, *49*(4), 576–583.